THE ASTROPHYSICAL JOURNAL SUPPLEMENT SERIES, 96:223–259, 1995 January

THE RIASS CORONATHON: JOINT X-RAY AND ULTRAVIOLET OBSERVATIONS OF NORMAL F–K STARS

THOMAS R. AYRES[1]
Center for Astrophysics and Space Astronomy, University of Colorado, Campus Box 389, Boulder, CO 80309; ayres@vulcan.colorado.edu

T. A. FLEMING[2]
Joint Institute for Laboratory Astrophysics, University of Colorado, Campus Box 440, Boulder, CO 80309

T. SIMON
Institute for Astronomy, University of Hawaii, 2680 Woodlawn Drive, Honolulu, HI 96822

B. M. HAISCH
Lockheed Palo Alto Research Laboratories, Division 91-30, Building 256, 3251 Hanover Street, Palo Alto, CA 94304

A. BROWN[3]
Joint Institute for Laboratory Astrophysics, University of Colorado, Campus Box 440, Boulder, CO 80309

D. LENZ
Center for Astrophysics and Space Astronomy, University of Colorado, Campus Box 389, Boulder, CO 80309

W. WAMSTEKER, D. DE MARTINO, AND C. GONZALEZ
ESA *IUE* Observatory, Apartado 50727, E-28080 Madrid, Spain

J. BONNELL
NASA *IUE* Observatory, Code 684.9, NASA-GSFC, Greenbelt, MD 20771

J. M. MAS-HESSE
Departmento de Astrofisica, Universidad Complutease, E-28040 Madrid, Spain

C. ROSSO, J. H. M. M. SCHMITT, J. TRÜMPER, AND W. VOGES
Max-Planck-Institut für Extraterrestrische Physik, D-8046 Garching bei München, Germany

J. PYE
Department of Physics and X-ray Astronomy Group, Leicester University, University Road, Leicester LE1 7RH, UK

R. C. DEMPSEY AND J. L. LINSKY[4]
Joint Institute for Laboratory Astrophysics, University of Colorado, Campus Box 440, Boulder, CO 80309

E. F. GUINAN
Astronomy Department, Villanova University, Villanova, PA 19085

G. M. HARPER, C. JORDAN, AND B. M. MONTESINOS
Department of Theoretical Physics, University of Oxford, 1 Keble Road, Oxford OX1 3NP, UK

AND

I. PAGANO AND M. RODONÒ
Istituto di Astronomia, Università di Catania, and Osservatorio Astrofisico, Viale Andrea Dorio 6, I-95125 Catania, Italy
Received 1993 September 24; accepted 1994 June 30

ABSTRACT

Between 1990 August and 1991 January the *ROSAT*/*IUE* All Sky Survey (RIASS) coordinated pointings by the *International Ultraviolet Explorer* with the continuous X-ray/EUV mapping by the *Röntgensatellit.* The campaign provided an unprecedented multiwavelength view of a wide variety of cosmic sources. We report findings for F–K stars, a large proportion of the RIASS targets. Forty-eight of our 91 "Coronathon" candidates were observed by the *IUE* during the campaign. For stars missed by the *IUE,* we supplemented the *ROSAT* survey fluxes with archival UV spectra and/or follow-on observations.

In addition to the coordinated work, we examined the UV emission histories of the Coronathon stars. Several of the dwarfs show evidence for long-term variations in their Mg II λ2802[*h*] emissions, and C IV λ1549 in a few cases. α Cen B (K0 V) and o^2 Eri (K1 V) are noteworthy examples. Hertzsprung gap giants like 31 Com (G0 III) and the secondary of Capella (α Aur Ab: G0 III) are relatively constant in C IV and Mg II, at least over decade timescales. Similarly, G8–K0 "Clump" giants show only modest long-term changes in their ultraviolet emissions. On the other hand, several of the "hybrid chromosphere" G and K supergiants show dramatic variability in the

[1] Guest Observer, *International Ultraviolet Explorer.*
[2] Visiting Scientist, Max-Planck-Institut für Extraterrestrische Physik.
[3] Visiting Scientist, SERC Rutherford Appleton Laboratory.
[4] Staff Member, Quantum Physics Division, National Institute of Standards and Technology.

wind absorption components of their Mg II *h* profiles. The closely related but more active G supergiants like β Cam and β Dra show smaller changes in their Mg II fluxes, and symmetric profile variations.

Despite clear indications of secular variability, we find little support for the suspicion that previous *broad statistical* X-ray/UV studies of normal stars have been compromised by nonsimultaneous data sets. For well-studied stars, the temporal standard deviation rarely exceeds 20% in C IV, and 10% in Mg II *h*. We find no evidence that long-term cycles play any significant role in fostering the large dispersion in activity within any of the stellar classes.

We correlated the X-ray and UV emissions, normalized to the stellar bolometric fluxes (e.g., $\mathscr{R}_X \equiv f_X/f_{\rm bol}$). As found by Ayres, Marstad, & Linsky, MS stars of spectral types *F–K* obey a power-law relation between $\mathscr{R}_X$ and $\mathscr{R}_h$ with a slope of ≈ 3. Here, the dwarf stars follow a $\mathscr{R}_{\rm C\,IV}$ versus $\mathscr{R}_h$ power law of slope ≈ 2, and a $\mathscr{R}_X$ versus $\mathscr{R}_{\rm C\,IV}$ power law of slope ≈ 1.5. The F9-G2 "solar-type" MS stars have a significantly steeper slope in X-rays versus C IV than the cooler G8–K5 dwarfs. The populous Clump giants follow essentially the same behavior as the cooler MS stars, showing a nearly 1:1 correlation between X-rays and C IV. However, other key groups—some F dwarfs, the Hertzsprung gap giants, and virtually all of the supergiants—fall systematically to lower $\mathscr{R}_X$ with respect to their $\mathscr{R}_{\rm C\,IV}$ and $\mathscr{R}_h$ (as noted previously by Simon & Drake for the former two classes), and exhibit steeper power laws than the cooler stars.

The MS and evolved stars detected in both X-rays and the WFC S1 and S2 filters show close to a 1:1 connection between their normalized coronal and EUV fluxes. Thus, the latter likely are dominated by $T > 10^6$ K emissions. There is no distortion in the X-ray/EUV diagram which would indicate that the "X-ray deficiency" of the F dwarfs or Hertzsprung gap giants is caused by local absorption at the source. All of the X-ray deficient stars follow a normal (i.e., MS) correlation between $\mathscr{R}_{\rm C\,IV}$ and $\mathscr{R}_h$, suggesting that the X-ray deficit truly is a coronal anomaly.

Many of the Clump giants, and G/K supergiants, show enhanced N V/C IV ratios, possibly associated with envelope enrichment of nitrogen at first dredge-up. C IV/C II ratios display a slight tilt toward larger values with increasing $\mathscr{R}_X$ in the dwarf stars, but a nearly 1:1 relation in the Clump giants. The origin of the effect is uncertain. O I/Mg II ratios exhibit a systematic increase in the more luminous objects. The origin likely is Bowen fluorescence. The "coronal proxy" He II λ1640 shows a near 1:1 correlation with X-rays in the MS stars as a function of $\mathscr{R}_{\rm C\,IV}$, but a more complex behavior among the giants, particularly the X-ray deficient stars. Curiously, He II shows a 1:1 correlation with Si IV among the X-ray deficient giants, displaced a factor of $\sim$2 below the relation obeyed by the Clump giants and cooler MS stars. These behaviors are consistent with recombination domination in the dwarfs and Clump giants, but the situation among the warm luminous stars is ambiguous.

The wide diversity of X-ray emission levels in the Clump—as exemplified by the Hyades K giants—emphasizes the sensitive role played by stellar evolution in controlling coronal activity. The wide diversity of X-ray emission in general points to a magnetic origin for the coronal heating.

Subject headings: stars: coronae — stars: chromosphere — stars: late-type — ultraviolet: stars — X-rays: stars

1. INTRODUCTION

In the mid 1970s the first direct X-ray detections of stellar coronae were made.[5] Initial discoveries were by sounding rockets (e.g., α Aur: Catura, Acton, & Johnson 1975). Later, the *Astronomy Netherlands Satellite* (Mewe et al. 1975) and *HEAO 1* recorded coronal sources in all sky surveys (e.g., Walter, Charles, & Bowyer 1978; Ayres et al. 1979). At the same time, ultraviolet coronal proxies were found in late-type stars by *Copernicus* (e.g., O VI λ1032: Dupree 1975) and the *International Ultraviolet Explorer* (e.g., C IV λ1549: Linsky & Haisch 1979 [hereafter LH]; Ayres, Marstad, & Linsky 1981 [hereafter AML]). These studies paved the way for the high-sensitivity X-ray pointings by *Einstein* at the turn of the decade. The *Einstein* era emphasized the remarkable diversity in coronal activity found among stars of a given spectral type and luminosity class. It clearly implicated magnetic activity as the driving force (e.g., Vaiana & Rosner 1978; Vaiana et al. 1981).

The central unifying theme was the *rotation-activity* connection. Rotation is important because it catalyzes the hydromagnetic Dynamo (Parker 1970). The Dynamo is the likely root of the cyclic, globally organized, although locally unpredictable magnetic activity seen on the surface of the Sun and presumably present on other stars as well.

For example, the photospheric spots and emission line activity of the BY Draconis variables were attributed by Bopp & Fekel (1977) to rapid rotation, enforced in the case of the binary BY Draconids by tidal synchronization. The prodigious X-ray/FUV activity of short-period RS CVn binaries was explained similarly by their fast synchronous rotation (Ayres & Linsky 1980; Middlekoop & Zwaan 1981). The "long-period RS CVn" Capella (α Aur: G8 III + G0 III) was shown to owe its anomalously intense C IV emission to the fast rotating G0 III star (Ayres & Linsky 1980). The latter is a rare Hertzsprung gap giant newly evolved from the upper MS, retaining the rapid rotation of its B-type progenitor. Noyes et al. (1984) identified a remarkable correlation between the Ca II emissions of MS stars and their rotation-dependent Rossby numbers, a critical parameter in Dynamo theories. Even the infamous "coronal dividing line" near K0 III, first discovered in C IV (LH) and subsequently recognized in X-rays, was attributed to rotation. Moderate-mass and low-mass post-MS trajectories converge in

[5] α Aur (Capella) appears to have been recorded in the 2 keV band more than a decade earlier by a gas proportional counter launched on an Aerobee rocket (Fisher & Meyerott 1964). However, the spatial resolution was too poor for a firm identification.

TABLE 1

PROPERTIES OF CORONATHON SAMPLE

HD	Name	Type	V	$B-V$	$V-R$	B.C.	d (pc)	Notes
			(a) F5–K5 Dwarfs					
148048	η UMi	F5 V	4.95	+0.37	[+0.36]	+0.08	23	···
134083	45 Boo	F5 V	4.93	+0.43	+0.40	+0.05	16	···
173667	110 Her	F6 V	4.20	+0.46	+0.39	+0.06	19	···
17206	τ^1 Eri	F6 V	4.46	+0.48	+0.43	+0.04	14	†
203608	γ Pav	F6 V	4.22	+0.48	+0.47	+0.01	8.5	···
142860	γ Ser	F6 IV	3.85	+0.48	+0.49	+0.00	12	···
154906,5	μ Dra AB	2×F7 V	4.92	+0.48	[+0.43]	+0.04	22	†
126660	θ Boo	F7 V	4.05	+0.50	+0.42	+0.04	14	···
222368	ι Psc	F7 V	4.13	+0.51	+0.45	+0.03	13	···
33262	ζ Dor	F7 V	4.72	+0.52	+0.48	+0.01	12	···
90839	36 UMa	F8 V	4.84	+0.52	+0.48	+0.01	13	†
142373	χ Her	F8 V	4.62	+0.56	+0.48	+0.01	16	···
102870	β Vir	F9 V	3.61	+0.55	+0.48	+0.01	9.6	···
22484	10 Tau	F9 V	4.28	+0.57	+0.49	+0.00	16	···
1581	ζ Tuc	F9 V	4.22	+0.57	+0.50	−0.01	7.1	···
114710	β Com	G0 V	4.26	+0.58	+0.49	+0.00	8.1	†
39587	χ^1 Ori	G0 V	4.41	+0.59	+0.51	−0.02	9.6	†
109358	β CVn	G0 V	4.27	+0.59	+0.54	−0.04	8.5	†
141004	λ Ser	G0 V	4.43	+0.60	+0.51	−0.02	11	†
19373	ι Per	G0 V	4.05	+0.60	+0.53	−0.03	11	···
212698,7	53 Aqr AB	G1+G3 V	5.56	+0.61	[+0.51]	−0.02	18	†
72905	π^1 UMa	G1 V	5.64	+0.62	+0.52	−0.02	14	⋆
128620	α^1 Cen	G2 V	−0.01	+0.71	[+0.57]	−0.06	1.3	†⋆
114613	HR 4979	G3 V	4.85	+0.70	+0.57	−0.06	19	···
32923	104 Tau	2×G4 V	5.01	+0.65	[+0.53]	−0.03	16	†
20630	κ^1 Cet	G5 V	4.84	+0.68	+0.57	−0.06	9.3	···
115617	61 Vir	G5 V	4.74	+0.71	+0.58	−0.07	8.5	···
117176	70 Vir	G5 V	4.98	+0.71	+0.61	−0.09	23	···
20794	HR 1008	G8 V	4.27	+0.71	+0.62	−0.10	6.2	†
10700	τ Cet	G8 V	3.50	+0.72	+0.62	−0.10	3.5	···
131156	ξ Boo A	G8 V	4.54	+0.77	+0.63	−0.11	6.4	†⋆
166	HR 8	K0 V	6.13	+0.75	[+0.60]	−0.08	15	†
185144	σ Dra	K0 V	4.69	+0.80	+0.65	−0.14	5.6	···
165341	70 Oph	K0 V [+K4 V]	4.03	+0.86	+0.65	−0.14	5.0	†
155886,5	36 Oph AB	K0+K1 V	4.32	+0.86	[+0.67]	−0.15	5.3	†
26965	o^2 Eri	K1 V	4.43	+0.82	+0.69	−0.17	4.8	†
10476	107 Psc	K1 V	5.24	+0.84	+0.69	−0.17	8.4	†
17925	HR 857	K1 V	6.05	+0.87	+0.71	−0.20	8.3	···
128621	α^2 Cen	K1 V	1.33	+0.88	[+0.69]	−0.17	1.3	†⋆
22049	ϵ Eri	K2 V	3.73	+0.88	+0.72	−0.21	3.3	†
16160	HR 753	K3 V	5.82	+0.97	+0.83	−0.33	7.8	†
219134	HR 8832	K3 V	5.56	+1.00	+0.83	−0.33	6.8	†
209100	ϵ Ind	K4 V	4.69	+1.06	+0.88	−0.40	3.4	···
201091,2	61 Cyg AB	K5+K7 V	4.81	+1.24	[+1.03]	−0.61	3.4	†
			(b) F5–K0 Giants					
71243	α Cha	F5 III	4.07	+0.39	[+0.37]	+0.08	19	···
1671	ρ And	F5 III	5.18	+0.42	[+0.39]	+0.06	[40]	···
48737	ξ Gem	F5 IV	3.36	+0.43	+0.39	+0.06	18	···
61064	25 Mon	F6 III	5.12	+0.44	[+0.40]	+0.06	[40]	†
35072	ζ Pic	F7 III-IV	5.45	+0.51	[+0.45]	+0.03	[40]	†
124850	ι Vir	F7 IV	4.09	+0.51	+0.50	−0.01	23	···
220657	υ Peg	F8 III-IV	4.41	+0.61	+0.54	−0.04	28	···
111812	31 Com	G0 III	4.94	+0.67	+0.55	−0.04	[90]	···
72779	35 Cnc	G0 III	6.58	+0.68	+0.54	−0.04	[190]	···
6903	ψ^3 Psc	G0 III	5.55	+0.69	[+0.56]	−0.05	[120]	···
223460	HR 9024	G1 III	5.90	+0.79	[+0.63]	−0.12	[140]	···
82210	24 UMa	G4 III-IV	4.57	+0.77	+0.66	−0.17	24	···
141714	δ CrB	G4 III	4.63	+0.80	+0.63	−0.12	[70]	···

TABLE 1—*Continued*

HD	Name	Type	V	$B-V$	$V-R$	B.C.	d (pc)	Notes
85444	υ^1 Hya	G7 III	4.11	+0.92	+0.69	−0.20	[50]	···
203387	ι Cap	G8 III	4.27	+0.91	+0.62	−0.11	[60]	···
115659	γ Hya	G8 III	3.00	+0.92	+0.60	−0.09	[35]	†
150997	η Her	G8 III	3.50	+0.92	+0.67	−0.17	29	···
113226	ϵ Vir	G8 III	2.84	+0.94	+0.64	−0.14	23	···
28307	θ^1 Tau	K0 III	3.83	+0.95	+0.71	−0.23	[45]	†
27371	γ Tau	K0 III	3.65	+0.99	+0.73	−0.25	[45]	⋆
27697	δ^1 Tau	K0 III	3.76	+0.99	+0.73	−0.25	[45]	†⋆
62509	β Gem	K0 III	1.14	+1.00	+0.75	−0.28	11	···
4128	β Cet	K0 III	2.02	+1.01	+0.72	−0.24	16	···
28305	ϵ Tau	K0 III	3.54	+1.01	+0.73	−0.25	[45]	⋆
			(c) Miscellaneous					
61421	α CMi	F5 IV	0.37	+0.42	+0.42	+0.04	3.4	†
121370	η Boo	G0 IV	2.68	+0.58	+0.44	+0.04	9.3	†
2151	β Hyi	G2 IV	2.80	+0.62	+0.50	+0.01	6.3	···
190248	δ Pav	G7 IV	3.56	+0.76	+0.61	−0.09	5.7	···
34029b	α Aur Ab	G0 III	0.76	+0.65	[+0.5]	−0.04	13	†
93497	μ Vel	G5 III	2.69	+0.90	+0.68	−0.19	[45]	†
34029a	α Aur Aa	G8 III	0.91	+0.88	[+0.7]	−0.16	13	†
36079	β Lep	G5 II	2.84	+0.82	+0.65	−0.10	[100]	†
109379	β Crv	G5 II	2.64	+0.88	+0.61	−0.07	[90]	···
31910	β Cam	G1 Ib-II	4.03	+0.93	+0.70	−0.16	[325]	†
159181	β Dra	G2 Iab:	2.78	+1.00	+0.68	−0.14	[180]	†
			(d) Hybrid Chromosphere Giants					
124897	α Boo	K1 III	−0.05	+1.23	+0.97	−0.62	10	···
81817	HR 3751	K3 III	4.30	+1.48	+1.13	−0.91	[70]	†
198700	β Ind	K1 II	3.65	+1.25	[+0.85]	−0.35	[170]	†
163770	θ Her	K1 IIa	3.87	+1.35	+0.90	−0.50	[190]	···
150798	α TrA	K2 II-III	1.92	+1.44	[+1.00]	−0.77	[75]	···
186791	γ Aql	K3 II	2.72	+1.52	+1.07	−0.77	[110]	†
31398	ι Aur	K3 II	2.69	+1.53	+1.06	−0.75	[110]	···
204867	β Aqr	G0 I	2.87	+0.84	+0.61	−0.07	[190]	†⋆
209750	α Aqr	G2 Ib	2.93	+0.97	+0.66	−0.12	[200]	†⋆
145544	δ TrA	G2 Ib-II	3.85	+1.11	[+0.75]	−0.21	[160]	†
			(e) RS Canum Venaticorum Binaries					
108102	IL Com	2×F8 V	8.16	+0.51	+0.40	+0.06	[90]	†
77137	TY Pyx	2×G5 IV	6.90	+0.68	[+0.59]	−0.08	[60]	†
106677	DK Dra	2×K0 III	6.29	+1.14	[+0.84]	−0.40	[130]	†

* From original miscellaneous category

166: $\Delta m = 2.6$ @ 2.″5
10476: $\Delta m = 6.4$ @ 0.″3
16160: SB (low-mass companion); $\Delta m = 5$, sep = 3″
17206: SB: 958^d
20794: G8 III in BSC
22049: $\Delta m = 3$, separation = 2″: 25 yr [?] astrom.
26965: $\Delta m = 5.0$, separation = 83″: 252 yr
27697: SB: 1.5 yr
28307: SB: $\gtrsim 10$ yr; $\Delta m > 3.8$
31910: $\Delta m = 3.4$ @ 1.″5
32923: $\Delta m = 0.1$, separation < 1″
34029: SB: 104^d
35072: luminosity class IV [Mg h]?
36079: $\Delta m = 4.5$ @ 3″
39587: low-mass companion
61064: $\Delta m = 5.3$ @ 2′
61421: $\Delta m = 10$ separation = 5″; 41 yr
77137: SB: $3.^d2$
81817: WD companion
90839: $\Delta m = 3.4$ @ 2′
93497: $\Delta m = 3.7$ separation = 2″; 116y
106677: SB: $63.^d8$
108102: SB: $0.^d8$
109358: SB1O: 2430^d
114710: SB? [>5 yr]; $\Delta m = 6$ @ 1.″5
115659: $\Delta m = 6.7$ @ 2′
121370: SB: 1.4 yr; $\Delta m = 6$ @ 2′
128620,1: $\Delta m = 1.4$, separation ≈ 20″; 81 yr
131156: $\Delta m = 2.1$, separation = 7″; 152 yr
141004: SB1O: 1837d
145544: $\Delta m = 8.0$ @ 0.″5
154906,5: $\Delta m = 0.1$, separation = 2″
155886,5: $\Delta m = 0.0$, separation = 5″; K0–SB
159181: $\Delta m = 8.9$ @ 4″
165341: $\Delta m = 1.8$, separation = 2″; SBO: 88y
186791: $\Delta m = 8.0$ @ 2′
198700: $\Delta m = 8.8$ @ 0.″3
201091,2: $\Delta m = 0.8$, separation = 29″
204867: $\Delta m = 7.9$ @ 0.″5
209750: $\Delta m = 9.0$ @ 2′
212698,7: $\Delta m = 0.2$, separation = 3″
219134: astrom.; $\Delta m = 3.8$ @ 1.″5

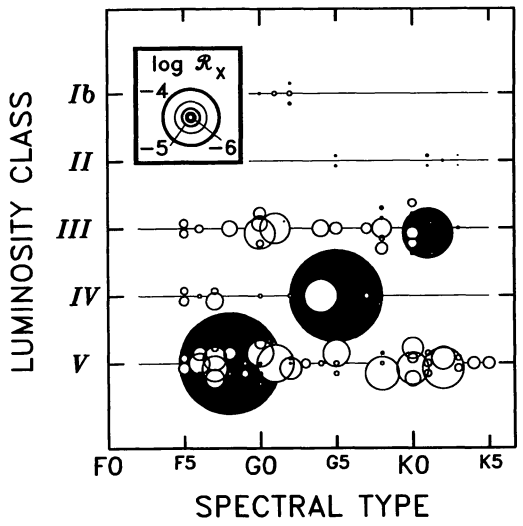

FIG. 1*a*

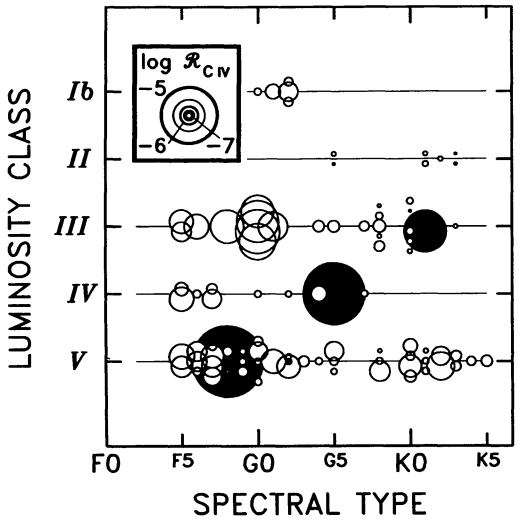

FIG. 1*b*

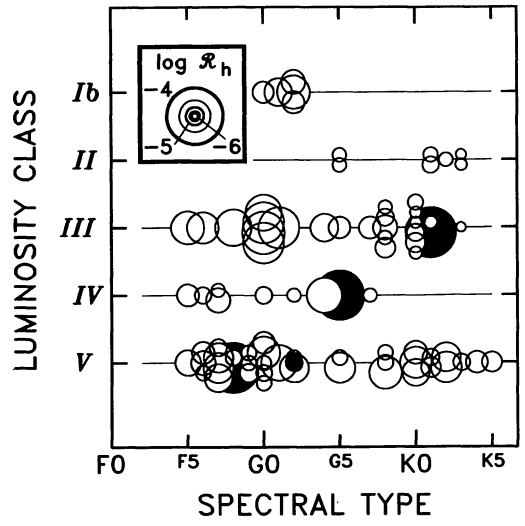

FIG. 1*c*

FIG. 1.—(*a*) Coronal H-R diagram of the Coronathon sample. The abscissa and ordinate indicate the MK classification. The size of the bubble is proportional to $\mathcal{R}_X \equiv f_X/f_{bol}$ according to the legend. The solid dot at G2 V represents the average Sun. The large shaded circles are (hyperactive) RS CVn binaries. (*b*) Same as (*a*) for the transition zone emission C IV λ1549. (*c*) Same as (*a*) for chromospheric Mg II *h*.

the red giant branch, populating neighboring regions with stars having very different angular momentum histories (Ayres et al. 1981; Haisch & Simon 1982).

In the decade following *Einstein,* only a few new coronal X-ray measurements were made. At the same time, there was considerable reflection upon the historical data.

For example, Simon & Drake (1989, hereafter SD) recognized a more subtle boundary in the coronal H-R diagram blueward of the sharp LH dividing line near K0 III. A precipitious drop in FUV emissions and rotation rates occurs redward of mid-F among the MS stars and G0 among the Hertzsprung gap giants (e.g., Gray 1991). The stars on the warmer side of the boundary not only lack a strong rotation-activity correlation, but they also exhibit a remarkable X-ray "deficiency" (with respect to C IV). SD attributed these phenomena to a transformation between predominantly acoustic coronal heating in the early-F dwarfs and Hertzsprung gap giants, and Dynamo-controlled coronae in the cooler G/K dwarfs and giants.

In parallel, the "coronal" giants of the core helium burning (CHeB) "Clump" received new scrutiny. The postflash late-G/early-K stars straddle the LH coronal dividing line and blur it. Most of the Clump giants are relatively inactive, aside from a few anomalous objects like β Cet (K0 III), θ^1 Tau (K0 III), and the G8 III primary of Capella (Ayres 1988). Apparently the first ascent of the giant branch can be traumatic for the Dynamo, but not for all stars.

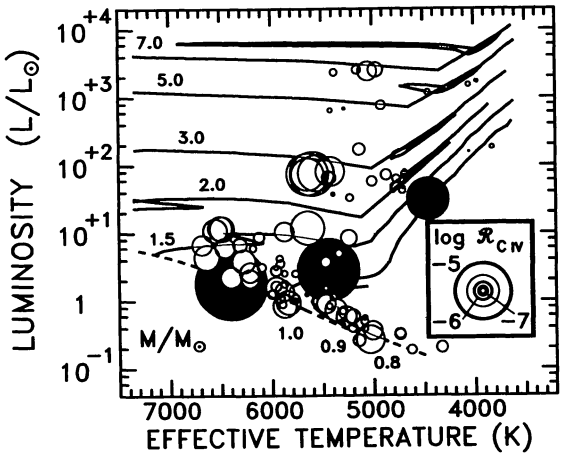

FIG. 2.—Same as Fig. 1*b*, but with MK class replaced by $\mathcal{L}/\mathcal{L}_\odot$ vs. T_{eff}. The solid curves are evolutionary tracks from Schaller et al. (1992). The zero age main sequence is dashed.

TABLE 2

RIASS INSTRUMENTS AND BANDPASSES

Band	Satellite	Inst.	Mode	$E/\Delta E$	Diagnostic	Bandpass[a]
X-ray	ROSAT	PSPC	Open	2.2	...	0.1 – 2.4 keV
EUV	ROSAT	WFC	S1	2	...	065 – 155 Å
			S2	2	...	110 – 195 Å
FUV	IUE	SW	LO	300	N V λ1241.0	8.2 ± 0.5 Å
					O I λ1304.6	7.0 ± 0.5 Å
					C II λ1334.9	5.8 ± 0.5 Å
					Si IV λ1393.2	5.5 ± 0.5 Å
					Si IV λ1402.3	7.5 ± 0.5 Å
					C IV λ1549.2	7.3 ± 0.5 Å
					He II λ1641.1	7.0 ± 0.5 Å
MUV	IUE	LW	HI	10^4	Mg II λ2802.7	1.3 Å [V]
						2.0 Å [III]
						3.2 Å [Ib]

[a] FWHM ± tolerance for FUV emissions; typical (luminosity class dependent) integration bandpass (Δλ) for Mg II *h*.

The Clump also harbors the unusual lithium-rich, fast rotating, coronally active single K giants (e.g., SD; Fekel & Marschall 1991; Fekel & Balachandran 1993). Such stars are difficult to assimilate within the broad evolutionary scenarios presented by Ayres et al. (1981), SD, and others. It is possible that some are coalesced binaries, or first crossers that avoided strong braking at G0. Another possibility is that their surface spins were "rejuvenated" at first dredge-up by angular momentum-rich material from their cores.

One encounters additional puzzles moving up in luminosity to the bright giants and supergiants. These massive stars ($M > 5\ M_\odot$) evolve on nearly horizontal trajectories from the upper main sequence. The post-MS timescales are very short compared with lower mass stars. The tracks can become quite convoluted sporting numerous "blue loops" in the F/G region. Some of the G-type supergiants like β Cam (G1 Ib–II) and β Dra (G2 Iab) are UV bright and X-ray active. Closely related stars like α Aqr (G2 Ib) and β Aqr (G0 I) are UV quiet and noncoronal. The latter, together with α TrA (K2 II-III), belong to the curious group of "hybrid chromosphere" giants (Hartmann, Dupree, & Raymond 1980, 1981). Such stars exhibit signs of X-ray emission (Brown et al. 1991; Haisch, Schmitt, & Rosso 1991; Reimers & Schmitt 1992) while expelling strong low-excitation winds. Signatures of coronal activity and cool winds tend to be mutually exclusive among the lower luminosity K-type giants (LH).

The exploration of the coronal "zoo" was revitalized at the beginning of the present decade by the *Röntgensatellit* (*ROSAT*). Not only did it comprehensively catalog the X-ray sky, but it also conducted extensive coordinated work with ground-based observatories and other space missions. One such opportunity was the *ROSAT*/*IUE* All Sky Survey (RIASS). It was organized by representatives of the *ROSAT* instrument teams and the *IUE Observatory,* under the overall direction of W. Wamsteker. Here we describe observations of a large minimally biased sample of F–K stars during the RIASS campaign and subsequent follow-up work, including a careful assessment of the historical material in the *IUE* Archives.

2. THE CORONATHON SAMPLE

Our objective was to extensively inventory the X-ray/UV emission properties of normal[6] late-type stars. We initially restricted our sample to single stars, or wide binaries, of spectral types F–K. Such stars are X-ray and C IV active, but their variability largely is on *rotational* timescales of at least days, if not weeks to months. The anticipated slow variations were an important consideration in scheduling the contemporaneous *IUE* pointings during RIASS.

The main part of the Coronathon consisted of two magnitude-limited groups: (*a*) F5–K5 dwarfs and (*b*) F5–K0 giants. All of the candidates are in the *Bright Star Catalogue* (Hoffleit & Jaschek 1982). Most have reliable parallaxes. We rejected objects known to be short period binaries ($P \lesssim 500$ d), for which tidal synchronization can upset the "normal" coronal evolution. We also rejected candidates with visual companions of $\Delta V \lesssim 5$ within $\sim 1'$, the nominal spatial resolution of the PSPC at low energies. (However, the effective FWHM of the PSPC ultimately realized in the survey was $\sim 2'$). We did include spectroscopic binaries with measured long-period orbits if there were strong indications that any low-mass companion (e.g., dMe) would not seriously contaminate the X-ray or C IV emissions of the visual primary. In a few cases we included a visual binary for which the components are nearly identical, the separation is small enough that it presents a point source target to the *IUE,* but the orbital period is long enough that synchronization is not a concern.

For the Clump giants ($\approx$G8–K0) we imposed the additional constraint of a measured C IV flux exceeding $\sim 1 \times 10^{-13}$ ergs cm^{-2} s^{-1}, if the candidate was fainter than $V = 3$. The Clump stars are a populous group, but they tend to be inactive. Most would be difficult targets for both *IUE* and ROSAT even with a generously bright limiting V.

[6] By "normal" we mean stars whose evolution is not unduly affected by their environment, i.e., isolated objects. Close binaries, for example, are *abnormal* because tidal torqing can influence the stellar spins, and in extreme cases Roche overflow can skew the component masses.

TABLE 3

A. *IUE* OBSERVATIONS OF F5–K5 DWARFS

HD No.	Name	Type	Archival Material SWP	LWP	LWR
		New Observations			
Image No.		t_{exp} (min:sec)	J.D. (2,448,000+)	Program	Observer
148048	η UMi	F5 V	✓	x	x
SWP 43990 L		90:00	667.4	CCNTA	Ayres
134083	45 Boo	F5 V	✓	✓	✓
LWP 19658 H		30:00	284.6	RIASS	Bonnell
SWP 40637 L		95:00	277.0†	MC180	Cassatella
173667	110 Her	F6 V	✓	x	✓✓
LWP 18855 H		18:00	158.1‡	RIASS	...
SWP 39698 L		45:00	158.1‡	RIASS	...
17206	τ^1 Eri	F6 V	✓	✓	x
LWP 19578 H		18:00	271.4†	RIASS	Bonnell
SWP 40592 L		75:00	271.4†	RIASS	Bonnell
203608	γ Pav	F6 V	✓	x	✓
142860	γ Ser	F6 IV	✓	✓	✓
154906,5	μ Dra AB	2×F7 V	✓	x	✓
SWP 39387 L		40:00	106.7†	RIASS	Bonnell
126660	θ Boo	F7 V	✓✓	x	✓
SWP 40329 L		25:00	239.9†	MC180	Cassatella
222368	ι Psc	F7 V	✓	✓	✓
LWP 19388 H		20:00	237.4†	RIASS	...
SWP 40310 L		125:00	237.3†	RIASS	...
33262	ζ Dor	F7 V	✓✓	✓	✓✓
LWP 19656 H		20:00	284.5	RIASS	Bonnell
SWP 40694 L		40:00	284.5	RIASS	Bonnell
90839	36 UMa	F8 V	✓	x	x
SWP 43973 L		225:00	665.3	CCNTA	Ayres
142373	χ Her	F8 V	✓✓	✓	✓✓
102870	β Vir	F9 V	✓✓	x	✓✓
LWP 19389 H		20:00	237.5†	RIASS	...
SWP 40307 L		65:00	236.9†	MC180	de Martino
22484	10 Tau	F9 V	✓	✓	✓
SWP 42341 L		120:00	496.8	CCNTA	Ayres
1581	ζ Tuc	F9 V	✓	x	✓
SWP 40060 L		65:00	201.6†	RIASS	Bonnell
114710	β Com	G0 V	✓✓	x	✓✓
SWP 40380 L		130:00	244.0†	MC180	Wamsteker
39587	χ^1 Ori	G0 V	✓✓	✓✓	✓✓
LWP 18764 H		25:00	146.7†	RIASS	...
SWP 39615 L		75:00	146.7†	RIASS	...
109358	β CVn	G0 V	✓	✓	✓✓
141004	λ Ser	G0 V	✓	✓	✓
SWP 42220 L		125:00	480.1	CCNTA	Ayres

TABLE 3A—*Continued*

HD No.	Name	Type	Archival Material SWP	LWP	LWR
	New Observations				
Image No.		t_{exp} (min:sec)	J.D. (2,448,000+)	Program	Observer
19373	ι Per	G0 V	√√	✓	√√
212698,7	53 Aqr AB	G1+G3 V	✓	✓	x
LWP 19235 H		40:00	212.7†	RIASS	Bonnell
SWP 40124 L		100:00	212.7†	RIASS	Bonnell
72905	π^1 UMa	G1 V	√√	√√	√√
LWP 18973 H		15:00	173.9‡	SAMEG	Dorren
LWP 18989 H		20:00	176.9	SAMEG	Dorren
SWP 39773 L		65:00	170.1†	MC180	Fernley
SWP 39798 L		90:00	174.0‡	SAMEG	Dorren
SWP 39813 L		90:00	176.9	SAMEG	Dorren
128620	α^1 Cen	G2 V	√√	✓	√√
LWP 18562 H		02:00	115.0†	RIASS	Bonnell
SWP 39441 L		23:00	115.0†	RIASS	Bonnell
114613	HR 4979	G3 V	✓	x	x
32923	104 Tau	2×G4 V	✓	x	x
SWP 43966 L		180:00	664.4	CCNTA	Ayres
20630	κ^1 Cet	G5 V	√√	√√	√√
115617	61 Vir	G5 V	✓	✓	✓
SWP 44029 L		185:00	673.2	CCNTA	Ayres
117176	70 Vir	G5 V	✓	x	x
SWP 43982 L		180:00	666.3	CCNTA	Ayres
20794	HR 1008	G8 V	√√	✓	√√
10700	τ Cet	G8 V	√√	√√	√√
131156	ξ Boo A	G8 V	√√	√√	√√
LWP 19606 H		25:00	276.9†	MC180	Cassatella
SWP 40635 L		90:00	276.8†	MC180	Cassatella
166	HR 8	K0 V	✓	x	√√
185144	σ Dra	K0 V	✓	x	x
SWP 42191 L		135:00	476.2	CCNTA	Ayres
165341	70 Oph	K0 V	√√	√√	√√
SWP 39630 L		45:00	148.5†	RIASS	Bonnell
155886,5	36 Oph AB	K0+K1 V	√√	x	✓
SWP 39571 L		140:00	137.0†	RIASS	Bonnell
26965	o^2 Eri	K1 V	✓	✓	✓
SWP 43957 L		190:00	663.3	CCNTA	Ayres
10476	107 Psc	K1 V	✓	x	x
SWP 42186 L		160:00	475.2	CCNTA	Ayres
17925	HR 857	K1 V	√√	√√	✓
SWP 40670 L		90:00	281.2‡	RIASS	Bonnell
128621	α^2 Cen	K1 V	√√	√√	√√
LWP 18561 H		03:00	115.0†	RIASS	Bonnell
SWP 39442 L		40:00	115.1†	RIASS	Bonnell

TABLE 3A—*Continued*

HD No.	Name	Type	Archival Material SWP	LWP	LWR
	New Observations				
Image No.		t_{exp} (min:sec)	J.D. (2,448,000+)	Program	Observer
22049	ϵ Eri	K2 V	√√	√√	√√
SWP 42234L		30:00	481.2	CSMTA	Ayres
16160	HR 753	K3 V	√	√	x
SWP 42211L		185:00	479.2	CCNTA	Ayres
219134	HR 8832	K3 V	√	x	x
SWP 42221L		140:00	480.2	CCNTA	Ayres
209100	ϵ Ind	K4 V	√√	√√	√√
201091,2	61 Cyg AB	K5+K7 V	√√	√	√√
SWP 40140L		185:00	215.0†	MC180	···

We then added a "miscellaneous" category *c* containing interesting late-type stars that failed for one reason or another to be included in the other categories. Among these are: nearby F/G subgiants; early-G supergiants; the Hyades Clump giants (aside from θ^1 Tauri which fell into category *b* by virtue of *V* and $f_{C\,IV}$); two bright spectroscopic binaries (α Aur, μ Vel) with G giant primaries and well-classified companions; and two MS binaries (α Cen, ξ Boo) with $\Delta V \approx 1$ and orbits below the PSPC resolution (but resolved by the *Einstein* or *ROSAT* HRIs). We divided Capella (α Aur) into its separate components (G8 III + G0 III), because the relative UV emissions are known from phase-resolved high-dispersion *IUE* spectroscopy, and the relative X-ray luminosities can be inferred indirectly (e.g., Ayres 1988; Ayres, Schiffer, & Linsky 1983).

Finally, we brought in two additional classes of objects for the present discussion. Category *d* contains selected hybrid chromosphere stars based on published *ROSAT* survey fluxes and pointings (Haisch, Schmitt, & Rosso 1991; Reimers & Schmitt 1992). We included the archetype "noncoronal" red giant α Boo (Arcturus: K1 III; Ayres, Fleming, & Schmitt 1991). Blue shifted absorption components in Mg II *h* and *k* and faint C IV emission (reported here) render Arcturus a legitimate member of the class. Category *e* contains selected short-period RS CVn binaries contributed by a separate RIASS program (Dempsey et al. 1993). The RS CVn's were limited to three systems containing companions of identical luminosity class and minimally differing spectral type. The hybrids (specifically α Boo) and the RS CVn's are examples of low activity and hyperactive objects, respectively. They serve as extremes within which to view the more normal stars of the Coronathon.

Table 1 describes the final sample. The 91 targets represent nearly 100 stars when the binaries of equal components are taken into account. In appropriate cases, class *c* targets are listed under their more natural categories (but their heritage is noted). We employed the BSC and the SIMBAD database to establish fundamental parameters. Distances were determined from a measured parallax if larger than 0".025, or from an estimated M_V for the MK type. Bolometric fluxes, f_{bol}, were calculated according to AML using the bolometric corrections listed in Table 1. The latter were based on Johnson (1966) for the measured Johnson $(V-R)$ color if available, or $(B-V)$ otherwise. No corrections for reddening were undertaken.

Figures 1*a*–1*c* illustrate emission H-R diagrams for X-rays, C IV, and Mg II. The symbols are positioned according to MK type and class, and sized according to the normalized flux ($\mathscr{R} \equiv f/f_{bol}$). Figure 2 depicts an analogous diagram for C IV in terms of $\mathscr{L}_{bol}$ vs. T_{eff}. In Figures 1 and 2 the RS CVn systems are shaded to call attention to their extreme behavior compared with single stars of the same temperature and luminosity. In Figure 2 note the concentration of the "F giants" near, but above, the MS; the cluster of early-G class-III giants in the middle of the Hertzsprung gap; the "Clump" of late-G/early-K giants between 2-3 $M_\odot$; and the exaggerated blue loops that develop beyond 5 $M_\odot$.

3. OBSERVATIONS

The *ROSAT* All Sky Survey (RASS) began on 1990 July 30 and continued until 1991 January 25. Further scans were obtained in 1991 August to compensate for data gaps during the initial period. The overall mission has been described by Trümper (1983, 1992). Details concerning the instrumental hardware and observing methods are in Cruddace et al. (1991).

In brief, the sky was scanned along lines of constant ecliptic longitude every 96 minutes with a 0.83 m Wolter type I X-ray telescope and a Position Sensitive Proportional Counter (PSPC; energy range: 0.1–2.4 keV). The co-aligned Wide Field Camera (WFC) recorded the softer EUV band (65–195 Å). The satellite orbit precessed 1° per day in order to cover the entire sky in 6 months. Minimum PSPC exposure ($\approx$600 s) was along the ecliptic and maximum exposure ($\approx 3 \times 10^4$ s) was at the ecliptic poles. A typical target was visible for $\sim$2 days in the PSPC and $\sim$5 days in the WFC.

TABLE 3

B. *IUE* OBSERVATIONS OF F5–K0 GIANTS

HD No.	Name	Type	Archival Material		
			SWP	LWP	LWR
		New Observations			
Image No.		t_{exp} (min:sec)	J.D. (2,448,000+)	Program	Observer
71243	α Cha	F5 III	✓	✓	x
LWP 18586 L		01:11	118.6†	RIASS	Bonnell
SWP 39463 L		50:00	118.6†	RIASS	Bonnell
1671	ρ And	F5 III	✓	✓	x
SWP 40545 L		110:00	264.2‡	RIASS	Bonnell
48737	ξ Gem	F5 IV	✓	x	x
SWP 39697 L		20:00	158.0†	RIASS	...
61064	25 Mon	F6 III	✓	✓✓	x
LWP 18983 H		70:00	175.8†	RIASS	...
SWP 39807 L		55:00	175.8†	RIASS	...
35072	ζ Pic	F7 III-IV	✓	x	✓
SWP 39504 L		95:00	124.8†	RIASS	Bonnell
124850	ι Vir	F7 IV	✓✓	x	✓
SWP 40636 L		35:00	276.9†	MC180	Cassatella
220657	υ Peg	F8 III-IV	✓	✓	✓
LWP 19420 H		20:00	241.8†	RIASS	Bonnell
SWP 40364 L		20:00	241.8†	RIASS	Bonnell
111812	31 Com	G0 III	✓✓	✓✓	✓✓
SWP 40330 L		20:00	240.0†	MC180	Cassatella
72779	35 Cnc	G0 III	✓	x	✓✓
SWP 39890 L		95:00	185.6†	RIASS	Bonnell
6903	ψ^3 Psc	G0 III	✓✓	✓✓	✓
SWP 40544 L		30:00	264.1	RIASS	Bonnell
223460	HR 9024	G1 III	✓✓	✓	x
LWP 19481 H		45:00	252.4†	RIASS	Bonnell
SWP 40463 L		105:00	252.4†	RIASS	Bonnell
82210	24 UMa	G4 III-IV	✓✓	✓	✓
LWP 18970 H		12:00	173.0†	RIASS	Bonnell
SWP 39793 L		65:00	172.9†	RIASS	Bonnell
SWP 39794 L		70:00	173.0†	RIASS	Bonnell
141714	δ CrB	G4 III	✓	x	✓
SWP 44028 L		190:00	673.0	CCNTA	Ayres
85444	υ^1 Hya	G7 III	✓	✓	✓
LWP 19249 H		50:00	215.6†	RIASS	Bonnell
LWP 19250 L		00:15	215.8†	RIASS	Bonnell
SWP 40145 L		90:00	215.7†	RIASS	Bonnell
203387	ι Cap	G8 III	✓	✓	✓
LWP 19073 H		30:00	192.3‡	MC180	Gonzalez
SWP 39974 L		15:00	192.3‡	MC180	Gonzalez
115659	γ Hya	G8 III	✓	x	✓
SWP 40538 L		85:00	262.8‡	MC180	Fernley
150997	η Her	G8 III	✓	x	✓

TABLE 3B—*Continued*

HD No.	Name	Type	Archival Material SWP	LWP	LWR
		New Observations			
Image No.		t_{exp} (min:sec)	J.D. (2,448,000+)	Program	Observer
113226	ϵ Vir	G8 III	✓	x	✓✓
SWP 44036L		265:00	674.1	CCNTA	Ayres
28307	θ^1 Tau	K0 III	✓✓	✓	✓✓
SWP 39503L		70:00	124.6†	RIASS	Bonnell
27371	γ Tau	K0 III	✓✓	✓	✓✓
27697	δ^1 Tau	K0 III	✓✓	✓	✓✓
62509	β Gem	K0 III	✓✓	✓✓	✓✓
SWP 39774L		105:00	170.2†	MC180	Fernley
4128	β Cet	K0 III	✓✓	✓✓	✓✓
LWP 19419H		10:00	241.8†	RIASS	Bonnell
SWP 40363L		35:00	241.7†	RIASS	Bonnell
28305	ϵ Tau	K0 III	✓✓	✓	✓✓

During the RIASS campaign, the *IUE* satellite provided supporting observations in the vacuum ultraviolet. It was used primarily in the 5 Å resolution mode of the far-ultraviolet spectrometer ("SWP-LO": 1150–2000 Å), and in the 0.3 Å resolution mode of the mid-ultraviolet spectrometer ("LWP-HI": 1900–3200 Å). Over the 6 month period, 454 spectra were recorded by the *IUE* totaling 669 hr of exposure time. One hundred twenty eight objects, ranging from planets to active galactic nuclei, were observed. Nearly half of the targets were cool stars. Further details of the *IUE* mission can be found in Boggess et al. (1978), and of RIASS in de Martino et al. (1991). Table 2 summarizes the characteristics of the instruments used in our program.

Unfortunately, only part of our sample ultimately was recorded by the *IUE* during RIASS. The observing time awarded by the NASA and ESA review panels was severely limited. We had to eliminate many of our fainter targets, reduce the SWP-LO exposures to the bare minimum to detect C IV, and curtail supporting LWP-HI observations except in a few cases. Thus, our original magnitude-limited sample became, in essence, peer review limited.

Of the 48 Coronathon targets observed by the *IUE* during RIASS, 75% were recorded *inside* the few day visibility window of the PSPC. Nevertheless, the RIASS observations should be considered *contemporaneous* rather than simultaneous. The *IUE* spectra were integrations of minutes to hours at a *specific point* during the visibility period, whereas the PSPC counts were accumulated in 15 s snapshots every 96 minutes for 2–3 days.

During the *IUE* 14th Episode, in 1991 August and 1992 February, we obtained new SWP-LO's of 16 Coronathon candidates missed during the RIASS program. Most of these had not been observed previously by the *IUE*. The remaining "non-RIASS" stars of the sample mostly had adequate archival SWP-LO material. Table 3 catalogs the *IUE* spectra acquired during the RIASS campaign, in the subsequent Coronathon follow-on, and from the *IUE* Archives. In addition to 78 new SWP exposures and 62 LWPs, we dearchived 900 historical SWP-LOs and 1300 LWR/P echellograms.

4. ANALYSIS

4.1. *The PSPC Survey*

The raw PSPC survey data was processed automatically by the *ROSAT* Standard Analysis Software System (SASS: Voges 1992). The SASS time tagged, gain corrected, and applied an attitude solution to each detected X-ray photon. The complete all sky data set was divided into 360 sectors, 2° in right ascension by 90° in declination. The SASS scanned each sector, deleting point sources found in the initial pass. The spatial distribution of the remaining photons was fitted with a spline surface to derive a smooth background. A maximum likelihood detection algorithm then was applied to the restored data. The 5′ radius detection circle contains 98% of the total flux of a point source (Hasinger 1985). Figure 3 illustrates a small patch of the survey centered on one of the bright Coronathon targets.

Sources above the likelihood threshold were included in the Master Source List (MASOL). Count rates were determined by dividing the total events above background by the effective integration time, corrected for telescope vignetting and dead time. Source positions in the MASOL were validated against SAO and Hubble Guide Star Catalog entries. The 95% confidence error is 0.5. The Coronathon list was compared to the MASOL, and matches within 1′ were accepted. The risk of false identifications is minimal (cf., Stocke et al. 1991).

The observed PSPC count rate can be transformed into an

TABLE 3

C. *IUE* OBSERVATIONS OF MISCELLANEOUS TARGETS

HD No.	Name	Type	Archival Material SWP	LWP	LWR
		New Observations			
Image No.		t_{exp} (min:sec)	J.D. (2,448,000+)	Program	Observer
61421	α CMi	F5 IV	√√	√√	√√
SWP 39799 L		04:00	174.1†	MC180	Monier
SWP 39801 L		04:00	174.2†	MC180	Monier
121370	η Boo	G0 IV	√√	x	√
2151	β Hyi	G2 IV	√√	√√	√√
190248	δ Pav	G7 IV	√√	√	√√
34029	α Aur A	[G8]+G0 III	√√	√√	√√
SWP 39570 L		01:00	137.0†	RIASS	Bonnell
93497	μ Vel	G5 III	√√	√	√√
LWP 19465 H		15:00	248.9†	MC180	...
SWP 40444 L		25:00	248.9†	MC180	...
36079	β Lep	G5 II	√	x	√√
SWP 42340 L		250:00	496.6	CCNTA	Ayres
109379	β Crv	G5 II	√√	x	√√
31910	β Cam	G1 Ib-II	√	x	√
SWP 39569 L		50:00	136.9†	RIASS	Bonnell
159181	β Dra	G2 Iab:	√√	√√	√√
LWP 18671 H		10:00	131.1†	RIASS	Bonnell
SWP 39543 L		20:00	131.1†	RIASS	Bonnell

TABLE 3

D. *IUE* OBSERVATIONS OF HYBRID CHROMOSPHERE STARS

HD No.	Name	Type	Archival Material SWP	LWP	LWR
		New Observations			
Image No.		t_{exp} (min:sec)	J.D. (2,448,000+)	Program	Observer
124897	α Boo	K1 III	√√	√√	√√
81817	HR 3751	K3 III	√	x	√
198700	β Ind	K1 II	√	x	√
163770	θ Her	K1 IIa	√√	√√	√√
150798	α TrA	K2 II-III	√√	√√	√√
LWP 18694 H		10:00	136.8†	RIASS	Bonnell
SWP 39568 L		70:00	136.8†	RIASS	Bonnell
186791	γ Aql	K3 II	√√	√√	√√
31398	ι Aur	K3 II	√√	√√	√√
LWP 18670 H		20:00	131.0†	RIASS	Bonnell
SWP 39541 L		120:00	130.9†	RIASS	Bonnell
204867	β Aqr	G0 I	√√	√√	√√
209750	α Aqr	G2 Ib	√√	√√	√√
145544	δ TrA	G2 Ib-II	√	√√	√

TABLE 3

E. *IUE* OBSERVATIONS OF RS CVn BINARIES

HD No.	Name	Type	Archival Material SWP	LWP	LWR
		New Observations			
Image No.		t_{exp} (min:sec)	J.D. (2,448,000+)	Program	Observer
108102	IL Com	2×F8 V	✓	✓	x
LWP 19377H		210:00	234.9†	MC180	de Martino
LWP 19378L		04:40	235.2†	MC180	de Martino
SWP 40294L		120:00	235.1†	MC180	de Martino
77137	TY Pyx	2×G5 IV	✓✓	✓✓	✓
LWP 19186H		60:00	205.7†	RIASS	Bonnell
LWP 19187H		60:00	205.7†	RIASS	Bonnell
LWP 19188H		60:00	205.8†	RIASS	Bonnell
LWP 19189H		60:00	205.9†	MC180	Cutispoto
LWP 19190H		60:00	206.0†	MC180	Cutispoto
LWP 19191H		60:00	206.1†	MC180	Cutispoto
LWP 19192H		90:00	206.2†	MC180	Cutispoto
LWP 19193H		90:00	206.3†	RIASS	Bonnell
LWP 19194H		90:00	206.4†	RIASS	Bonnell
LWP 19195H		90:00	206.5†	RIASS	Bonnell
LWP 19196H		90:00	206.6†	RIASS	Bonnell
LWP 19197H		90:00	206.7†	RIASS	Bonnell
LWP 19198H		90:00	206.8†	RIASS	Bonnell
LWP 19199H		90:00	206.9†	MC180	Cutispoto
LWP 19200H		90:00	207.0†	MC180	Cutispoto
LWP 19201H		90:00	207.1†	MC180	Cutispoto
LWP 19202H		90:00	207.2†	RIASS	Bonnell
LWP 19203H		90:00	207.3†	RIASS	Bonnell
LWP 19204H		90:00	207.4†	RIASS	Bonnell
LWP 19205H		90:00	207.5†	RIASS	Bonnell
LWP 19206H		90:00	207.7†	RIASS	Bonnell
LWP 19207H		60:00	207.8†	RIASS	Bonnell
LWP 19208H		90:00	207.9†	RIASS	Bonnell
LWP 19209H		90:00	208.0†	MC180	Cutispoto
LWP 19210H		90:00	208.1†	MC180	Cutispoto
LWP 19211H		90:00	208.2†	MC180	Cutispoto
LWP 19212H		90:00	208.3†	RIASS	Bonnell
LWP 19213H		90:00	208.4†	RIASS	Bonnell
LWP 19214H		90:00	208.5†	RIASS	Bonnell
LWP 19215H		90:00	208.6†	RIASS	Bonnell
LWP 19216H		70:00	208.7†	RIASS	Bonnell
LWP 19217H		75:00	208.8†	RIASS	Bonnell
LWP 19218H		90:00	208.9†	RIASS	Bonnell
SWP 40092L		30:00	205.7†	RIASS	Bonnell
SWP 40093L		90:00	205.8†	MC180	Cutispoto
SWP 40094L		90:00	206.0†	MC180	Cutispoto
SWP 40095L		90:00	206.3†	RIASS	Bonnell
SWP 40096L		90:00	206.6†	RIASS	Bonnell
SWP 40097L		120:00	207.0†	MC180	Cutispoto
SWP 40098L		120:00	207.3†	RIASS	Bonnell
SWP 40099L		40:00	207.6†	RIASS	Bonnell
SWP 40100L		120:00	207.9†	MC180	Cutispoto
SWP 40101L		120:00	208.3†	RIASS	Bonnell
SWP 40102L		110:00	208.6†	RIASS	Bonnell
106677	DK Dra	2×K0 III	✓✓	✓	✓
LWP 19045H		30:00	185.5‡	RIASS	Bonnell
SWP 39889L		75:00	185.5‡	RIASS	Bonnell

NOTES TO TABLE 3.—For each star, the first line provides identifying information and a summary of *IUE* archival material. Subsequent lines refer to new *IUE* observations obtained either during the RIASS epoch or 6 months to a year later in follow-up work. Suffix on the image number indicates high dispersion (H) or low dispersion (L). J.D. refers to start of exposure. A single dagger indicates that the exposure was within the PSPC visibility window. A double dagger indicates that the exposure was within 3 days of the outer limits of the PSPC visibility. The dates of the PSPC passes can be found in de Martino et al. 1991. Archival material was restricted to SWP-LO and LW-HI large aperture observations. Archival spectra are enumerated as follows: x = none available (or accessible); ✓ = 1–3; ✓✓ = ≥4. "Observer" was taken from corresponding entry (if present) in Merged Catalog of Observations.

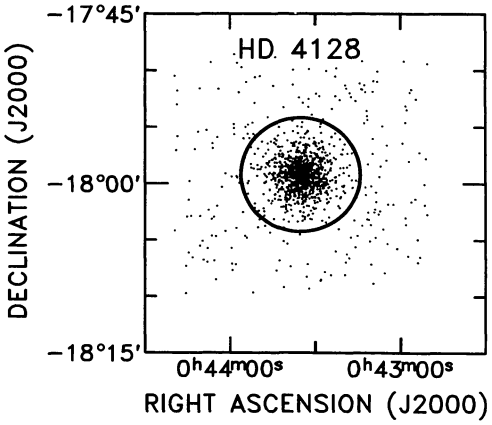

FIG. 3.—PSPC survey in vicinity of bright RIASS target HD 4128 (= β Cet). The circle represents the 5′ radius detection "window." Events outside it mostly are from the diffuse cosmic X-ray background.

X-ray flux by means of a spectrum-dependent energy conversion factor (ECF: in ergs cm^{-2} count^{-1}). Relatively hard sources like RS CVn binaries and dMe flare stars have an ECF of 8×10^{-12}. Softer solar-like sources have an ECF of only 3×10^{-12} (owing primarily to the excellent low-energy response of the PSPC). The conversion factor also depends on the line-of-sight absorption. Soft sources with large hydrogen columns can have large ECFs.

Most of the Coronathon targets are relatively nearby with minimal N_H. Only a few, however, were bright enough in the RASS for a reliable spectral analysis. Figure 4 depicts the pulse height distribution resulting from one such target. Because the coronal temperatures mostly are unknown, we adopted a uniform ECF of 5.5×10^{-12}. It corresponds to an isothermal Raymond-Smith spectrum for log $T = 6.35$ and negligible interstellar absorption (log $N_H < 19$; see *ROSAT* Mission Description [1991]. We thus accept an implicit systematic error of as much as 0.25 dex in addition to the photometric uncertainty.

We compared the derived RASS fluxes to *Einstein* IPC values for 27 stars in common with the Schmitt et al. (1990) survey of coronal temperatures. Excluding one discrepant value, the ratio of the PSPC to IPC fluxes was 1.1 with a dispersion of ±0.13 dex. The latter jibes with the expectation discussed above. It also suggests that the typical long-term variability of the coronal sources probably is small. The discrepant object was Procyon (α CMi: F5 IV), a very soft source. Our "uniform" ECF is a factor of nearly 2 high compared with the nominal soft ECF. Even the latter might be significantly overestimated (Napiwotzki et al. 1993).

4.2. *The WFC Survey*

Pounds et al. (1993) have described the techniques used to extract sources and assign count rates in the *ROSAT* WFC survey. The S1 and S2 EUV filter bands are very sensitive to interstellar absorption. Only nearby bright sources were detected, mostly hot white dwarfs and coronal late-type stars. In addition to the detections and upper limits reported in the "Bright Source List," we analyzed the WFC survey material at the positions of the Coronathon targets closer than 20 pc. We sought weak sources that might have been missed in the conservative all-sky inventory, and assigned upper limits where appropriate. A description of the procedure can be found in Wood et al. (1994).

4.3. *IUE SWP-LO*

4.3.1. *Calibration and Measurement of Individual Spectrograms*

We applied a state-of-the-art reduction to the SWP-LO material. Details concerning the flat fielding and the assignment of photometric errors through a "noise model" can be found in Ayres (1993). Following linearization of the raw vidicon frames, cosmic-ray hits were removed using an automated procedure. An off-spectrum background was derived by spatially filtering the counts in reference bands above and below the spectral swath. The net spectrum was extracted using an "Optimal" weighted slit (e.g., Kinney, Bohlin, & Neill 1991).

A dispersion relation was determined from well exposed SWP-LOs of the RS CVn star λ And (G8 III-IV: see, e.g., Bennett & Ayres 1988). The zero point of the wavelength scale varies owing to thermal shifts and/or miscenterings of the target. It was established according to reference stellar emissions, if visible, or geocoronal Lyα otherwise.

SWP-LO spectrograms of late-type stars are affected by grating scattered light (Basri, Clarke, & Haisch 1985). It affects the flux distribution below 1500 Å, particularly for the warmer stars whose photospheric continua rise steeply longward of 1700 Å. The scattered light level was estimated according to the average counts below the 1150 Å cutoff of the camera window. We subtracted the scattered light assuming it to be independent of wavelength.

The absolute calibration was based on the hot white dwarf G191-B2B, a fundamental flux standard for the *IUE*

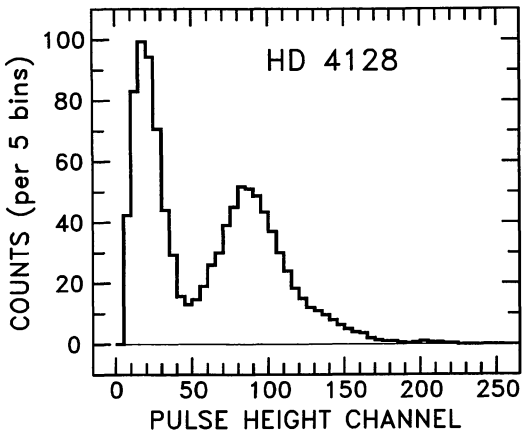

FIG. 4.—Smoothed PSPC pulse height distribution of HD 4128. The energy conversion is ≈ 10 eV per channel. The pronounced dip near channel 50 is due to absorption by carbon in the PSPC window. The spectrum is relatively hard, like those of RS CVn systems.

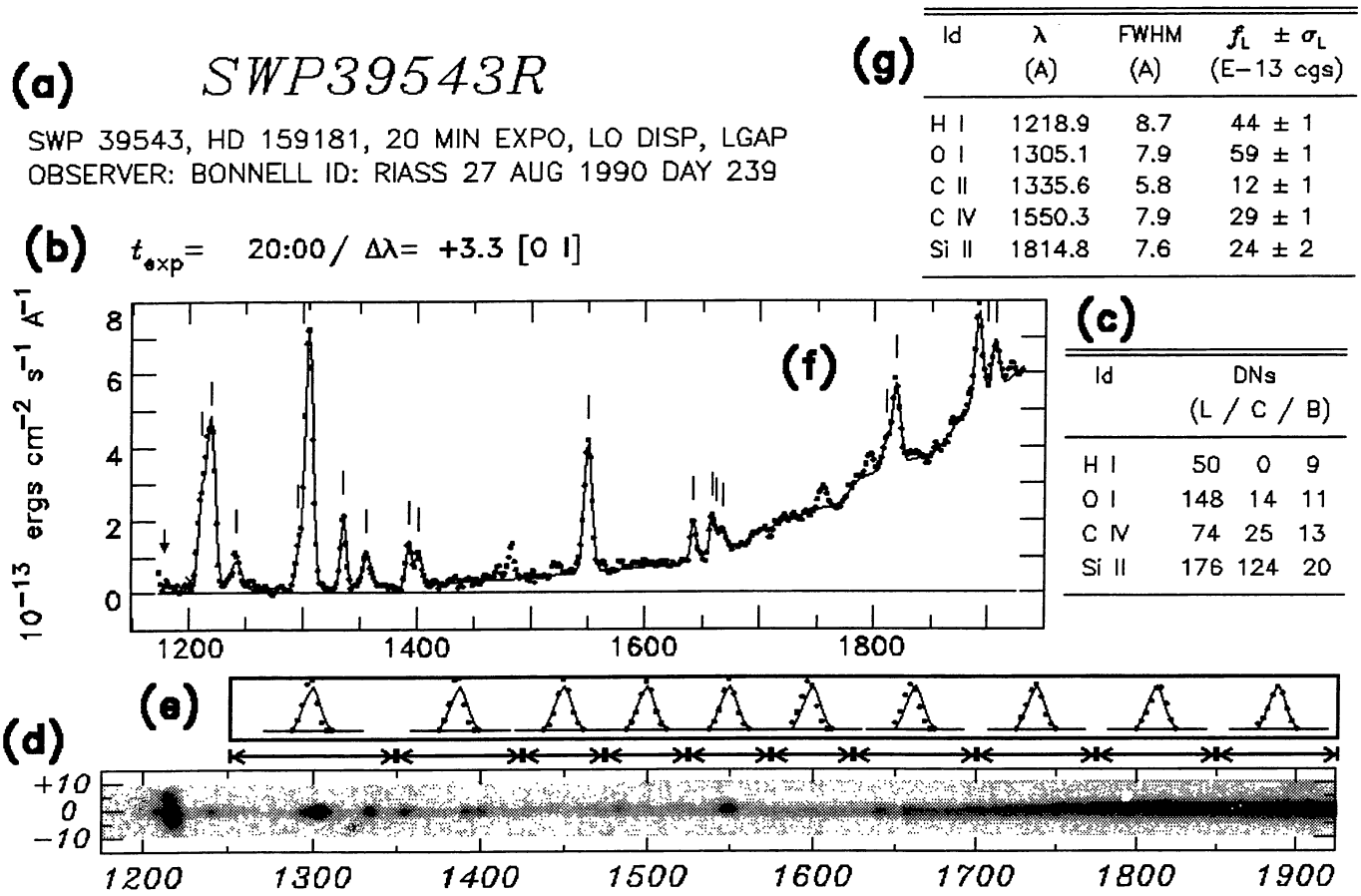

FIG. 5.—SWP-LO reduction procedure for RIASS spectrum of HD 159181 (= β Dra): (*a*) descriptive information from image header; (*b*) exposure time and zero point wavelength shift; (*c*) data numbers measured in raw image; (*d*) stretched version of photometrically linearized and background subtracted image (the faint "blob" near 1216 Å is diffuse Lyα emission filling the large aperture; white spots are reseau marks); (*e*) empirical cross-dispersion profiles (*dots*) of the "optimal" procedure in discrete wavelength bands indicated by arrows (solid curves are "global" profile); (*f*) calibrated spectrum (*dots*) and numerical fit (*solid curve:* ticks indicate detections, arrows indicate upper limits); and (*g*) selected measurements.

(Oliversen, Perez, & Garhart 1991). The reference theoretical energy distribution kindly was provided by D. S. Finley of the University of California at Berkeley. The absolute accuracy of the calibration is believed to be better than ±10% longward of 1400 Å, possibly as good as ±5%. The relative accuracy is significantly better than ±10%.

Each spectrum was measured by a semiautonomous line finding and fitting algorithm (Bennett 1987; Bennett & Ayres 1988). The constrained multiple Gaussian modeling considered 32 lines divided into 20 groups (blends) of 1–4 features each. (However, we report only the results for six key emissions from the interval λ < 1650 Å; see Table 2). The statistical significance of a fit was based on Lenz & Ayres (1992). Upper limits were set according to the local photometric uncertainty. The reduction procedure is illustrated in Figure 5.

4.3.2. *Co-addition of SWP-LO Spectrograms*

Many of the Coronathon targets have been observed more than once in the SWP-LO mode. The archival collections for popular stars like α Cen A can number 70 or more images. For each suitable star, we selected the deepest exposures, adjusted each in wavelength according to the derived zero point shift, and summed them. We weighted each spectrum by an average variance ($1/\langle\sigma^2\rangle$) in the interval 1500–1600 Å. The weighting factor usually is dominated by the photometric uncertainties contributed ultimately by the camera *background.* It is the fairest way to compare exposures of different lengths with perhaps radically different radiation fogging. We did not compensate for the thermal response or the wavelength dependent secular sensitivity decline of the SWP camera (Bohlin & Grillmair 1988). The two effects are small compared with the random photometric errors. The co-added spectra were measured as in the initial reduction. The weighted rms divided by the square root of the number of images served as an empirical estimate of the local flux uncertainty. Figure 6 depicts the procedure. Figures 7*a*–7*h* illustrate examples of the fitted spectra.

4.4. *IUE LW-HI*

Long-wavelength *IUE* echelle spectra are valuable for recording the Mg II λλ2795[*k*],2802[*h*] resonance doublet. It is

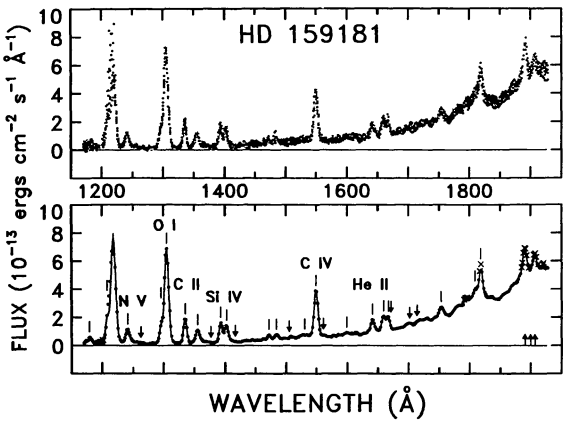

FIG. 6.—SWP-LO co-addition procedure, again for HD 159181. The upper panel overlays eight reduced SWP-LOs, including the RIASS observation. Exposure times range from 20 to 60 minutes. The lower panel compares the weighted sum (*dots*) and numerical fit (*solid curve*). Identified features are those reported in Table 4.

the most easily measured of the dominant radiative coolants of the T $\lesssim 10^4$ K chromosphere (Linsky & Ayres 1978). We considered only high-dispersion spectra. It is notoriously difficult to pry useful Mg II fluxes from LW-LOs.

The Mg II features usually are well exposed and normally cover many vidicon pixels. They are less affected by "fixed pattern noise" than low-resolution FUV spectra (see Ayres 1993). Thus, the standard *IUE* Spectral Image Processing System (IUESIPS; Turnrose & Thompson 1984) reductions were sufficient for our purposes. We postprocessed echelle orders m = 80–84 with blaze constants and radiometric calibrations available from the *IUE* Data Analysis Center. Unfortunately, the IUESIPS does not assign photometric uncertainties.

Mg II fluxes usually are measured by numerically integrating between the outer edges of the emission core, chosen by eye (e.g., AML). Figure 8 illustrates an example of such a measurement. Here, we adopted a modified strategy to avoid "subjective" errors in Mg II *h* flux sequences. We selected from the accessible LW-HI echellograms of a star a subset that were well exposed but not saturated, and not affected by high backgrounds. We corrected each profile for the camera thermal response and secular sensitivity degradation using the coefficients reported by Garhart (1992). The corrections are much larger for LWR, in particular, than for SWP, and potentially can mitigate otherwise significant systematic errors. We registered each profile to a common wavelength scale by cross-correlating against a template. We co-added the registered profiles to obtain a high-quality composite, using it to determine an integration window by eye. Finally, we applied the selected numerical integration uniformly to all of the Mg II profiles in the set. The internal errors should be dominated by the photometry, not by the uncertainty of placing integration windows in each spectrum individually. The scenario is illustrated in Figure 9. We minimized subjective errors over the entire Coronathon sample by adopting, to the extent possible, uniform integration bandpasses within the distinct stellar classes (see Table 2).

An important by-product was the ability to assign an empirical "photometric error" according to the rms deviation of the individual profiles from the mean. The bin-wise standard deviation sets an *upper limit* to the typical photometric errors, given the expectation of intrinsic chromospheric variability. If more than five profiles were available we applied an "Olympic" filter, discarding the high and low values in each wavelength bin. It avoids prejudicing the rms in favor of transient localized profile anomalies like cosmic-ray hits or LWR "pings." We derived a flux error from the standard deviation for the particular integration bandpass and assigned it to all of the measurements of the set.

We report here only the *h*-line flux. It is the weaker of the doublet components, but it is less affected by interstellar and circumstellar absorptions. The companion *k* line also can be corrupted by a unfortunately positioned reseau mark in LWP-HI. Figures 10*a*–10*h* display examples of single LW-HI exposures of the Coronathon stars.

4.5. *Summary of Measured Fluxes*

Table 4 summarizes the *ROSAT* and *IUE* fluxes.

For the PSPC we present fluxes and errors derived using the uniform ECF described previously. We did not augment the errors to reflect the uncertainty in the ECF. For the WFC we present the results in counts ks^{-1}. We did not attempt to derive ECFs for the S1 and S2 bands because the conversions are highly dependent on the uncertain hydrogen columns. Wood, Brown, & Linsky (1995) describe how the WFC fluxes can be combined with X-ray detections to constrain coronal temperatures, emission measures, and N_H.

For the FUV emissions we present the measurements from the *co-added* SWP-LO spectra, rather than the RIASS observations (if available). The relatively short RIASS exposures were designed to achieve a bare minimum detection of the bright C IV feature. Fainter emissions like N V λ1241 usually were not recorded adequately. Furthermore, co-added spectra are more reliable than single exposures. Finally, we have found for representative stars (see § 5.1, below) that the temporal standard deviations of the C IV and Mg II *h* fluxes tend to be small. We did, however, visually check each of the fitted co-added spectra. In a few cases where we felt that a fit was fortuitously good, we doubled the assigned error and flagged it in the table. The intent was to lessen the weight of questionable detections.

For the Mg II *h* line we provide either the RIASS flux, if an LWP-HI had been taken, or the average of the archival spectra otherwise. In contrast to the RIASS SWP-LOs, the LWP-HIs normally were well exposed. We assigned an error to the *h*-line flux of either 1 σ deviation of the historical fluxes, in the case of a RIASS measurement; or 2 σ for a non-RIASS flux (the 95% confidence level for long-term temporal fluctuations).

5. DISCUSSION

5.1. *Temporal Variability*

A key issue in coronal studies is the influence of nonsimultaneity in comparisons of X-ray and UV fluxes obtained in different epochs. For dMe stars and RS CVn binaries that flare frequently, one clearly wants measurements that are strictly

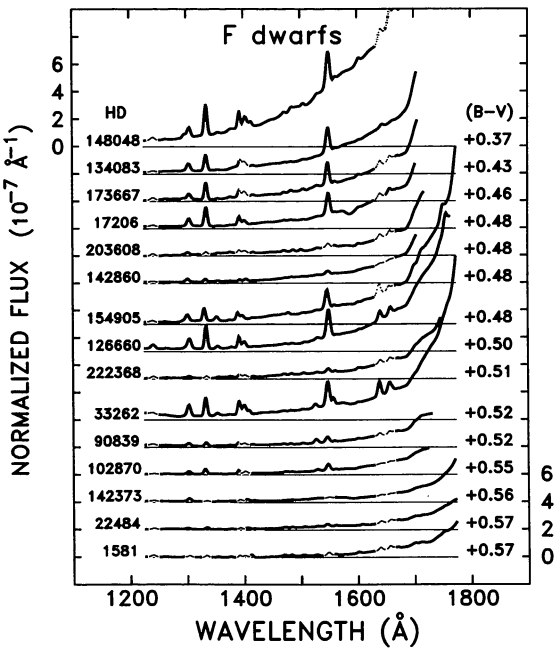

FIG. 7*a*

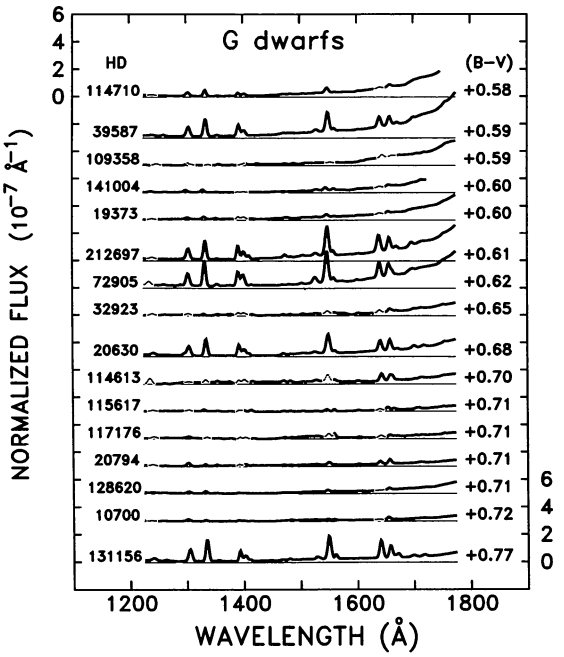

FIG. 7*b*

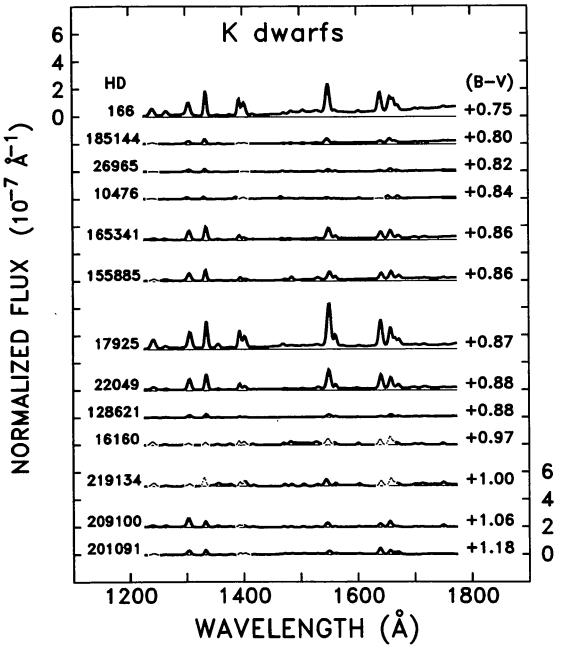

FIG. 7*c*

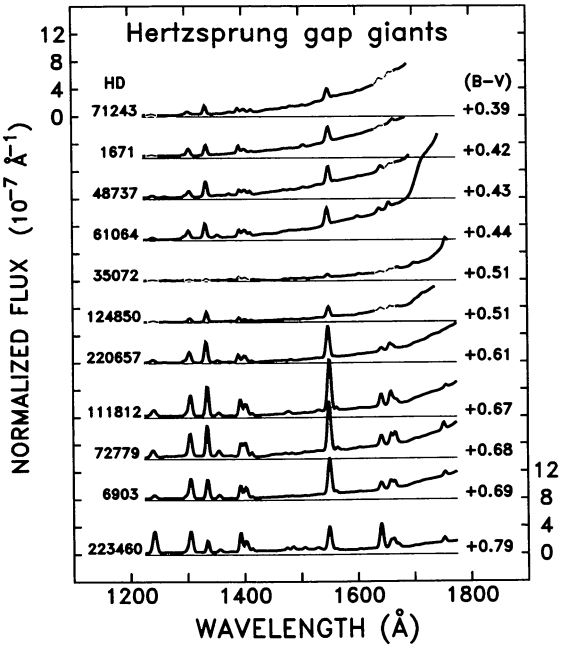

FIG. 7*d*

FIG. 7.—(*a*) FUV spectra of Coronathon F dwarfs. The ordinate is $f_\lambda/f_{\rm bol}$ (Å^{-1}). The traces depict *numerical fits* to the co-added spectra. Thinner (*dotted*) lines represent upper limits. The curves are truncated if the co-added spectrum was saturated. The stars are ordered from top to bottom in increasing $B-V$. Note the many stars with strong C IV, and the growth of the $\lambda > 1700$ Å photospheric continuum toward the bluer stars. (*b*) Same as (*a*) for G dwarfs. There are fewer examples of strong C IV, and the photospheric continua are less pronounced. (*c*) Same as (*a*) for K dwarfs. Again, fewer cases of strong C IV, and the photospheric continua are minimal. (*d*) Same as (*a*) for mid-F-early-G "Hertzsprung gap" giants. Note scale change from previous figures. C IV is strong in most of the objects. Significant continuum emission appears in the warmer stars. N V λ1241 and He II λ1640 are weak (with respect to C IV) in all of the stars except the reddest, HD 223460. (*e*) Same as (*a*) for mid-G-K0 "Clump" giants. Note scale change. Chromospheric O I λ1305 is prominent, while C IV is weak in most of the stars. However, N V and He II tend to be comparable in strength to C IV. (*f*) Same as (*a*) for "miscellaneous" targets. HD 61421 (= α CMi) is a nearby F subgiant. HD 2151 (= β Hyi) is an inactive G subgiant perhaps analogous to the future Sun. HD 34029 (= α Aur) is dominated by the G0 III secondary in the FUV. HD 93497 (= μ Vel) is an active Clump giant. A widely separated early-G MS companion accounts for the elevated photospheric continuum. HD 31910 (= β Cam) and HD 159181 (= β Dra) are active G supergiants. (*g*) Same as (*a*) for hybrid chromosphere stars including HD 124897 (= α Boo). As in the Clump giants, O I dominates the spectrum and the high-temperature lines tend to be weak. HD 81817 has a warm white dwarf companion that contributes a faint continuum throughout the FUV (Reimers 1984). (*h*) Same as (*a*) for RS CVn binaries. Note scale change. The RS CVn's represent the upper tier of cool star activity. Their FUV spectra are resplendent with prominent high-excitation emissions.

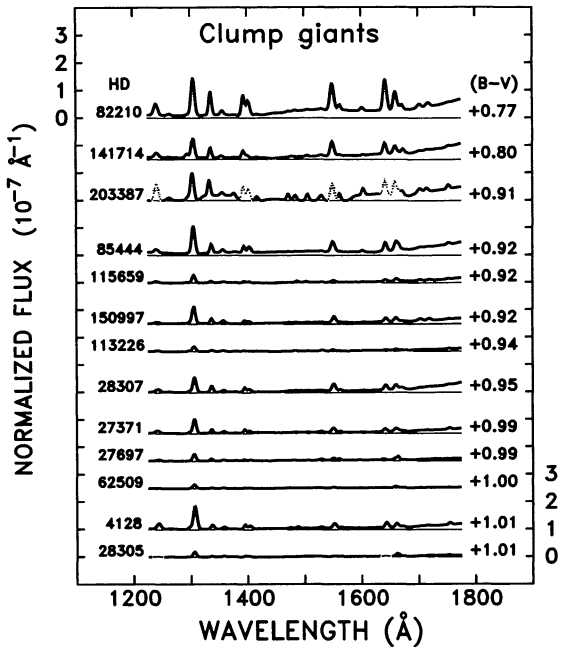

FIG. 7*e*

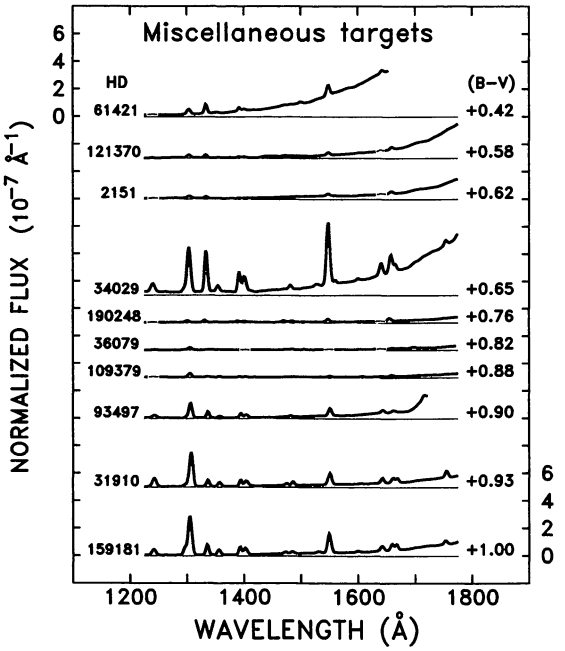

FIG. 7*f*

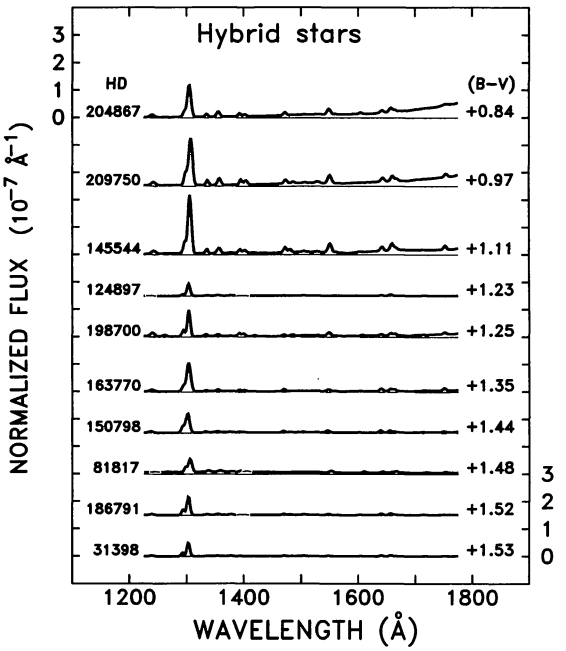

FIG. 7*g*

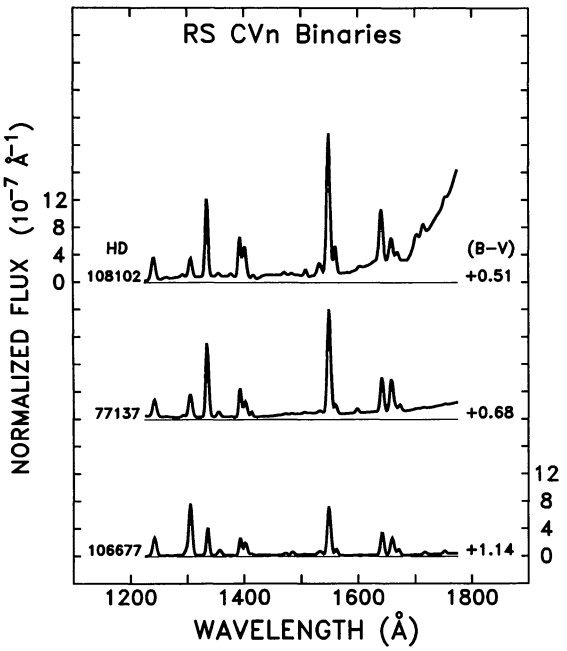

FIG. 7*h*

simultaneous. For less active stars, like the Sun, one in principle can relax the criterion. Now with 15 years of *IUE* observations, we can assess more quantitatively the question of variability, at least on the UV side.

We selected from the overall sample two subsets of stars well represented in either the SWP-LO or the LW-HI collections. Figures 11*a*–11*d* illustrate the C IV time histories of the SWP group. Figures 12*a*–12*g* depict the Mg II *h*-line histories of the LW group. Displayed in each panel is the average profile and the extreme excursions. Here, we corrected for time and temperature effects for both SWP and LWR/P, and applied an Olympic filter bin by bin.

In the C IV series one sees many examples of overt variability, particularly on short *rotational* timescales within intensive campaigns (e.g., Hallam & Wolff 1981; Boesgaard & Simon 1984; Hallam, Altner, & Endal 1991). The modulation ampli-

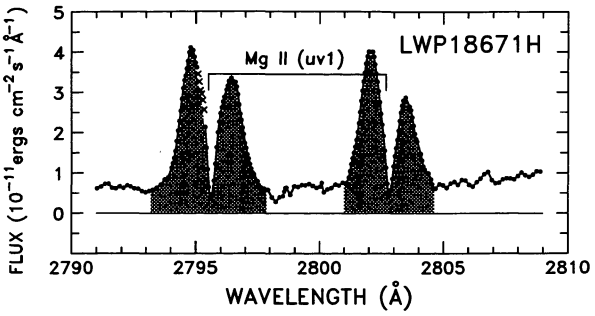

FIG. 8.—LWP-HI spectrum of HD 159181 from standard IUESIPS processing. The Mg II *h* and *k* emissions lie at the bottom of a broad absorption trough. The narrow dips in the emission cores probably are mostly interstellar. The shaded areas represent the flux in each component that we would ascribe to genuine chromospheric emission (see Linsky & Ayres 1978). Crosses flag a reseau mark on the inner shoulder of the *k*-line core.

tudes are surprisingly similar for the active and quiet stars. They are comparable to Sun's behavior during sunspot cycle 21 recorded by the Solar Mesosphere Explorer (Bennett 1987).

There are a few noteworthy exceptions. α Cen B has shown a remarkable decline in its C IV flux since 1986. The long-term change possibly indicates a magnetic cycle like those seen (on other stars) in Ca II monitoring programs (e.g., Baliunas & Vaughan 1985). The Hyades K giant θ^1 Tau appears to have suffered a significant dip in 1986. On the other hand, G0 giants like 31 Com, ψ^3 Psc, and Capella are remarkably constant, despite their high $\mathscr{R}_{\rm C\,IV}$'s.

The G supergiants α Aqr and β Dra both show relatively constant behavior. So do the K-type hybrids α TrA and γ Aql aside from a few possibly anomalous points. Kashyap et al. (1994) recently reported a large X-ray flare on α TrA during a deep *ROSAT* pointing. If coronal flares are common on the hybrids, they might affect some of the UV fluxes.

The RS CVn system TY Pyx was intensively monitored during the RIASS campaign. Like the cool dwarfs, it shows significant short-term (rotational) variations in C IV. Finally, some of the hotter dwarfs (e.g., ζ Dor and χ^1 Ori) exhibit significant deviations in their λ1550 *continuum* fluxes (cf., Simon, Herbig, & Boesgaard 1985; Böhm-Vitense & Mena-Werth 1991).

Even though the fluctuations tend to be smaller, the Mg II *h* time histories can be more revealing than those of C IV. One can follow changes in the line *shapes* as well as in the integrated fluxes. The hotter dwarfs show relatively little chromospheric variability, although there is a hint of an activity minimum in the ζ Dor record and possibly also in that of κ^1 Cet. The cooler dwarfs display more exaggerated short-term changes in the *h* line. A similar effect was noted by Wilson (1978) in his long-term study of the Ca II H and K emissions of late-type stars. α Cen B mimics the same rise/decline in the post-1986 era seen in C IV, while ϵ Eri experienced an almost sawtooth wave of variability over the 1980–1987 period.

Capella again appears to be quite steady although the profile varies enormously due to the binary orbit. There is a slight decline in the *h*-line flux. However, the calibration of the secular degradation of the cameras might be responsible, rather than the star. μ Vel shows a large apparent rise in the 1978–1982 time frame, while β Gem was very steady over that period. The active Clump giant β Cet has been essentially constant over periods of short-term monitoring. However, its *h*-line flux dipped a bit between 1986 and the RIASS epoch, suggestive of a stellar cycle. The Hyades K giants have been comparatively constant except for a low value for γ Tau in 1986 (the Olympic filter eliminated that profile from the lower bound in the left-hand panel).

In contrast, the hybrid giants (including α Boo) have exhibited considerable *h*-line variability. In the case of Arcturus, the Mg II flux and profile were relatively steady over the period 1978–1983. Sometime between then and 1988, however, the blue peak in the wind absorption trough brightened by a factor of 2. The other hybrids also have displayed significant variability of their wind absorptions over timescales of hundreds of days (as noted in previous work: see, e.g., Hartmann et al. 1985), and perhaps α TrA was caught flaring in Mg II in 1982. ι Aur has suffered the largest *h*-line fluctuations of the group. The red peak was affected as well as the wind trough. The G-type hybrids α Aqr and δ Tra have exhibited large changes in their wind absorptions, while β Aqr has been relatively "quiet." The apparent variability emphasizes the stochastic nature of mass loss in the cool supergiants.

β Dra is similar to the hybrid G supergiants in its fundamental properties aside from activity (Schmidt, Rosendhal, & Jewsbury 1974; Luck 1978). However, its profile variations are small, symmetrically distributed in wavelength, and without circumstellar involvement.

Figure 12*g* depicts the *h*-line time histories of several other interesting objects from the Coronathon. β Hyi has been one of the most closely watched stars by the *IUE* (Dravins et al. 1993). However, the early enthusiasm of the investigators (or review panels) appears to have waned in recent years. LWR observations of β Hyi were continued even after the nominal retirement of the camera to backup status in 1984. The more recent LWR-HIs diverge in their *h*-line fluxes compared with contemporaneous LWP-HI's. The agreement is good, how-

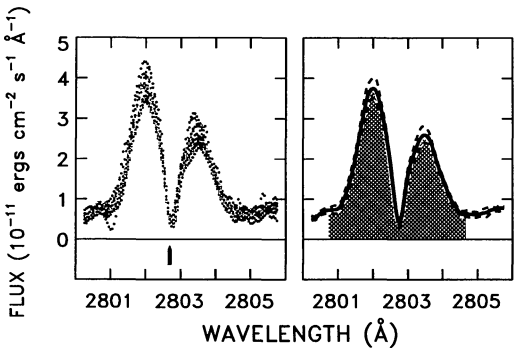

FIG. 9.—Mg II *h* measurement scheme. The left-hand panel overlays 13 LW-HI *h*-line spectra of HD 159181, registered in wavelength against a template profile. The large tick denotes the nominal line center. The right-hand panel illustrates the co-added profile. The dashed curve is ±1 σ. The hatched area indicates the limits of the numerical integration, chosen by eye. It then was applied uniformly to all of the registered profiles of the sequence.

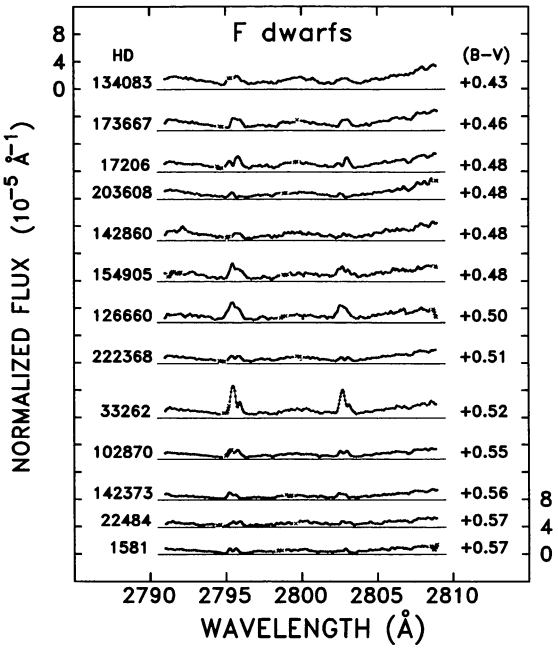

FIG. 10*a*

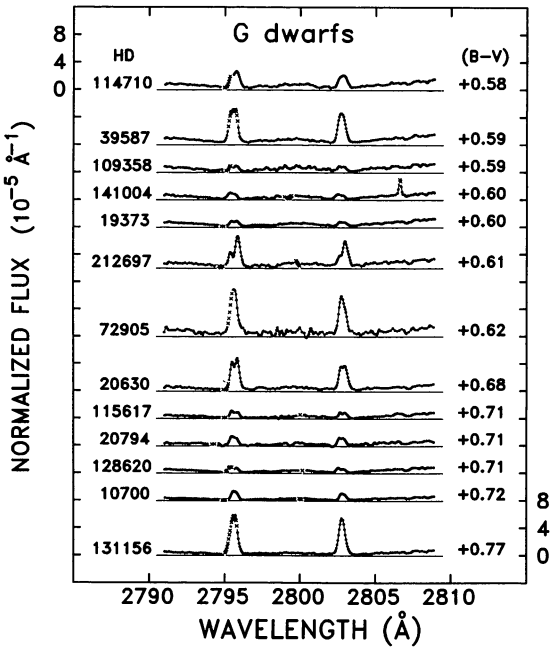

FIG. 10*b*

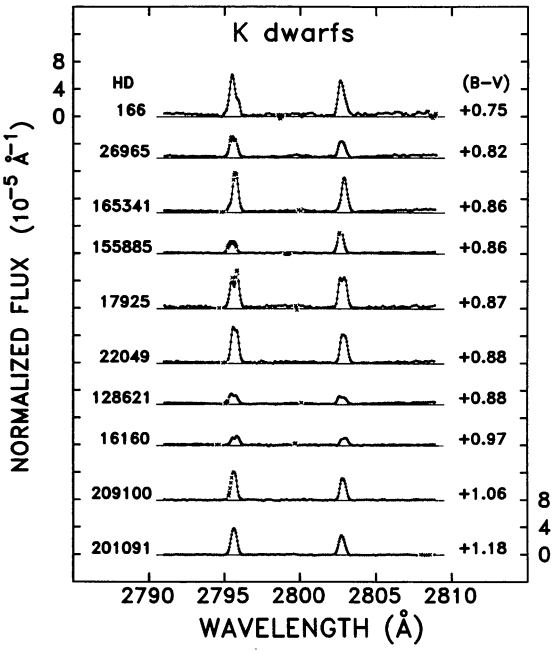

FIG. 10*c*

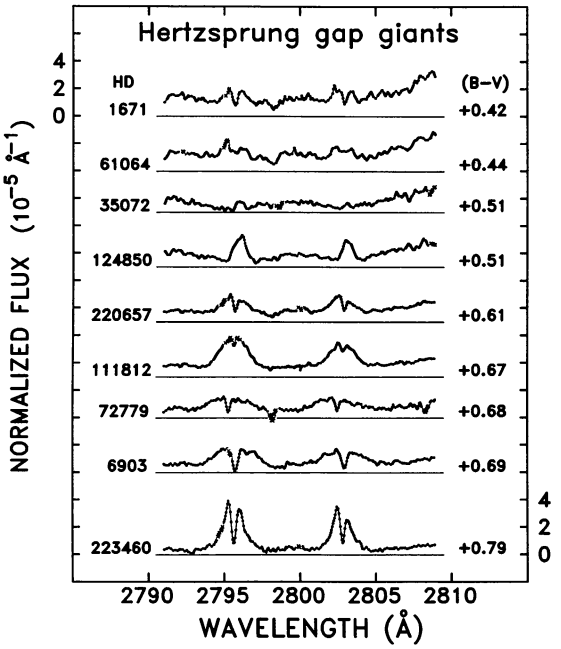

FIG. 10*d*

FIG. 10.—(*a*) Observed Mg II resonance lines of Coronathon F dwarfs. Preference was given to the RIASS LWP-HI if available. Crosses flag reseau marks or saturation. The inner portions of the extensive photospheric damping wings are visible in many cases. (*b*) Same as (*a*) for G dwarfs. The line wings are less prominent in the cooler stars. Narrow spikes (e.g., near 2807 Å in HD 141004) mostly are due to cosmic rays. (*c*) Same as (*a*) for K dwarfs. The photospheric wings are barely visible, and the line cores have narrowed slightly. (*d*) Same as (*a*) for Hertzsprung gap giants. The line wings are visible again, and the line cores mostly are quite broad (cf., Wilson & Bappu 1957). The narrow emissions of HD 35072 (= ζ Pic) are more appropriate to a subgiant than a giant. As in (*d*), HD 223460 is discrepant compared with other early-G giants. (*e*) Same as (*a*) for Clump giants. The emission cores are broader than those of the MS stars, but narrower than those of the (fast-rotating) Hertzsprung gap giants. (*f*) Same as (*a*) for miscellaneous targets. HD 34029 was observed near $\phi = 0.75$ when the secondary component was to the red and the primary component was to the blue (see, e.g., Ayres 1988). The profiles of the G supergiants HD 31910 and HD 159181 are quite broad as expected from the W-B Effect. (*g*) Same as (*a*) for hybrid stars. Notice the complex absorption profiles on the blueward side of the emission cores caused by low-excitation mass outflows. (*h*) Same as (*a*) for RS CVn binaries. The profile shapes are dominated by the orbital motions of the companions (cf., Capella in *f*). The components of HD 77137 (= TY Pyx) are completely split for example.

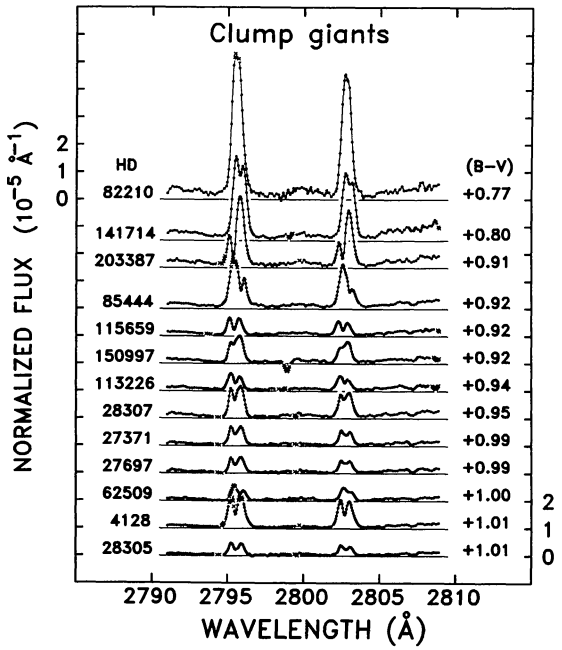

FIG. 10*e*

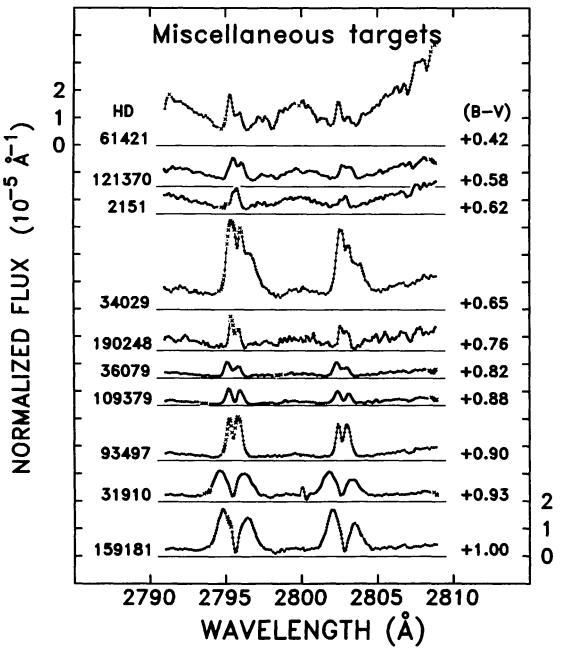

FIG. 10*f*

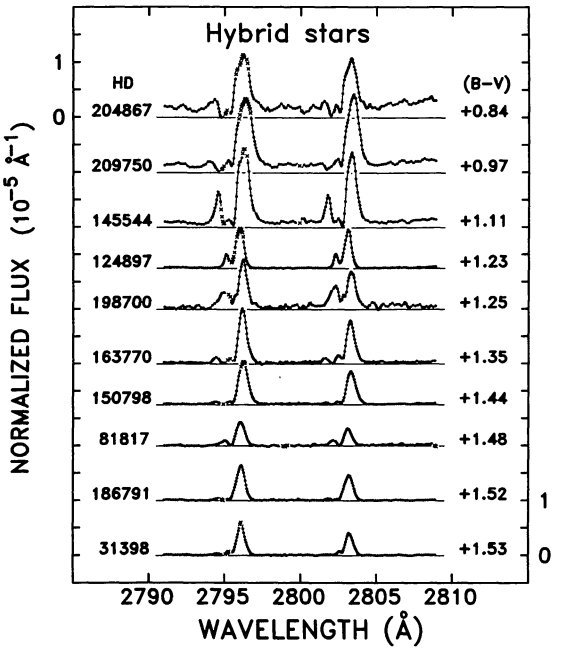

FIG. 10*g*

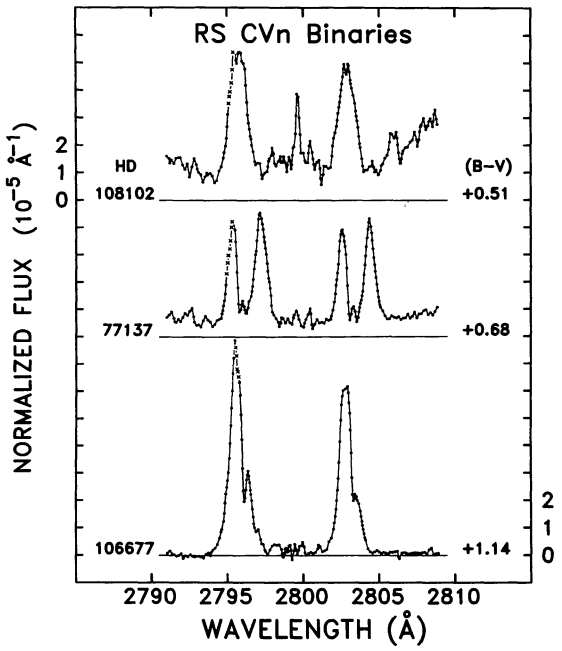

FIG. 10*h*

ever, during the camera swap in 1984. Discounting the recent LWR-HIs, the long-term variations of the ancient Sun analog are modest.

The RS CVn system TY Pyx displays large profile distortions, mostly due to orbital motions. Nevertheless, significant rotational modulations of the *h*-line flux occurred during the RIASS campaign. Since 1982, o^2 Eri has dramatically increased its *h*-line flux, suggestive of a large amplitude cycle. The *h*-line flux of another K dwarf—ϵ Ind—sharply rose in 1982. It remained stable, however, over the next 5 years of intermittent observation.

Table 5 summarizes the temporal standard deviations of the time series illustrated in the previous figures. The well-observed stars have rms deviations normally less than 20% in C

TABLE 4

A. *ROSAT* AND *IUE* FLUXES OF F5–K5 DWARFS

HD No. Type Name	f_X $f_{N\ V}$	f_{S1} $f_{O\ I}$	f_{S2} $f_{C\ II}$	$f_{C\ IV}$ $f_{Si\ IV}$	$f_{Mg\ II\ h}$ [$\Delta\lambda$ (Å)] $f_{He\ II}$
148048 F5 V	0.52 ± 0.16	$\lesssim$ 9	$\lesssim$ 9	0.516 ± 0.047	...
η UMi	$\lesssim$ 0.047	0.140 ± 0.014	0.375 ± 0.016	0.349 ± 0.029	$\lesssim$ 0.133
134083 F5 V	1.09 ± 0.20	$\lesssim$ 15	$\lesssim$ 18	0.382 ± 0.024	5.7 ± 0.3 [1.5]
45 Boo	$\lesssim$ 0.018	0.113 ± 0.014	0.198 ± 0.010	0.120 ± 0.048	0.040 ± 0.012
173667 F6 V	2.90 ± 0.20	$\lesssim$ 12	$\lesssim$ 15	0.637 ± 0.051	8.3 ± 0.4 [1.3]
110 Her	$\lesssim$ 0.079	0.151 ± 0.023	0.397 ± 0.024	0.245 ± 0.041	$\lesssim$ 0.157
17206 F6 V	5.70 ± 0.80	$\lesssim$ 21	$\lesssim$ 21	0.522 ± 0.023	7.9 ± 0.5 [1.4]
τ^1 Eri	$\lesssim$ 0.029	0.171 ± 0.017	0.386 ± 0.009	0.250 ± 0.060	$\lesssim$ 0.099
203608 F6 V	$\lesssim$ 0.20	...	...	$\lesssim$ 0.120	3.9 ± 0.6 [1.3]
γ Pav	$\lesssim$ 0.069	0.074 ± 0.019	$\lesssim$ 0.055	$\lesssim$ 0.099	$\lesssim$ 0.118
142860 F6 IV	0.28 ± 0.08	...	...	0.148 ± 0.040:	6.7 ± 0.6 [1.3]
γ Ser	$\lesssim$ 0.038	0.130 ± 0.013	0.092 ± 0.016	0.164 ± 0.060:	$\lesssim$ 0.037
154906,5 2×F7 V	3.00 ± 0.20	7 ± 3	5 ± 3	0.292 ± 0.025	6.9 ± 0.8 [1.7]
μ Dra AB	$\lesssim$ 0.025	0.101 ± 0.030:	0.151 ± 0.030:	0.143 ± 0.050:	$\lesssim$ 0.168
126660 F7 V	10.80 ± 0.40	26 ± 4	23 ± 4	1.040 ± 0.062	17.0 ± 1.0 [1.7]
θ Boo	0.146 ± 0.050:	0.358 ± 0.027	0.621 ± 0.050	0.474 ± 0.034	0.291 ± 0.050:
222368 F7 V	0.58 ± 0.09	$\lesssim$ 24	$\lesssim$ 27	0.121 ± 0.038	5.4 ± 0.2 [1.3]
ι Psc	$\lesssim$ 0.066	0.056 ± 0.018	$\lesssim$ 0.054	0.101 ± 0.032	$\lesssim$ 0.118
33262 F7 V	7.00 ± 0.40	20 ± 5	31 ± 7	0.479 ± 0.024	9.9 ± 0.5 [1.3]
ζ Dor	$\lesssim$ 0.025	0.209 ± 0.011	0.290 ± 0.014	0.406 ± 0.029	0.263 ± 0.013
90839 F8 V	1.55 ± 0.16	$\lesssim$ 15	$\lesssim$ 18	0.093 ± 0.030:	...
36 UMa	$\lesssim$ 0.024	0.043 ± 0.010:	0.055 ± 0.010:	0.049 ± 0.020:	$\lesssim$ 0.043
142373 F8 V	$\lesssim$ 0.20	...	...	$\lesssim$ 0.016	3.0 ± 0.2 [1.3]
χ Her	$\lesssim$ 0.017	0.060 ± 0.010:	$\lesssim$ 0.013	$\lesssim$ 0.034	$\lesssim$ 0.014
102870 F9 V	1.90 ± 0.20	14 ± 4	6 ± 6	0.321 ± 0.026	10.5 ± 0.2 [1.3]
β Vir	$\lesssim$ 0.023	0.132 ± 0.013	0.217 ± 0.015:	0.191 ± 0.018	$\lesssim$ 0.021
22484 F9 V	$\lesssim$ 0.17	...	...	0.064 ± 0.020	3.7 ± 0.6 [1.3]
10 Tau	$\lesssim$ 0.034	0.027 ± 0.009	0.047 ± 0.009	$\lesssim$ 0.047	$\lesssim$ 0.057
1581 F9 V	$\lesssim$ 0.38	...	...	$\lesssim$ 0.089	3.8 ± 0.6 [1.3]
ζ Tuc	$\lesssim$ 0.056	$\lesssim$ 0.045	$\lesssim$ 0.043	$\lesssim$ 0.074	$\lesssim$ 0.089
114710 G0 V	1.90 ± 0.20	9 ± 4	$\lesssim$ 15	0.148 ± 0.017	8.0 ± 1.3 [1.3]
β Com	$\lesssim$ 0.020	0.107 ± 0.009	0.145 ± 0.012	0.143 ± 0.018	$\lesssim$ 0.035
39587 G0 V	10.50 ± 0.52	36 ± 5	2 ±	0.515 ± 0.014	15.8 ± 0.6 [1.3]
χ^1 Ori	0.028 ± 0.010:	0.248 ± 0.009	0.402 ± 0.012	0.401 ± 0.014	0.250 ± 0.011
109358 G0 V	$\lesssim$ 0.20	...	...	$\lesssim$ 0.020	4.5 ± 0.5 [1.3]
β CVn	$\lesssim$ 0.045	$\lesssim$ 0.024	$\lesssim$ 0.014	$\lesssim$ 0.022	$\lesssim$ 0.083
141004 G0 V	0.20 ± 0.06	$\lesssim$ 12	$\lesssim$ 18	0.073 ± 0.020:	3.3 ± 0.4 [1.3]
λ Ser	0.023 ± 0.007	0.048 ± 0.005	0.056 ± 0.006	$\lesssim$ 0.012	$\lesssim$ 0.025
19373 G0 V	0.11 ± 0.04	...	...	0.091 ± 0.019	4.5 ± 0.4 [1.3]
ι Per	$\lesssim$ 0.027	0.056 ± 0.007	0.075 ± 0.007	$\lesssim$ 0.098	$\lesssim$ 0.036
212698,7 G1+G3 V	2.40 ± 0.21	$\lesssim$ 36	$\lesssim$ 33	0.274 ± 0.012	4.4 ± 0.1 [1.3]
53 Aqr AB	$\lesssim$ 0.014	0.094 ± 0.007	0.139 ± 0.013	0.175 ± 0.013	0.159 ± 0.014
72905 G1 V	6.60 ± 0.50	15 ± 5	12 ± 5	0.273 ± 0.013	6.2 ± 0.5 [1.3]
π^1 UMa	$\lesssim$ 0.034	0.099 ± 0.007	0.180 ± 0.013	0.192 ± 0.013	0.126 ± 0.014
128620 G2 V	5.40 ± 0.10[a]	123 ± 10[a]	248 ± 14[a]	2.500 ± 0.071	197 ± 6 [1.3]
α^1 Cen	0.507 ± 0.200	2.560 ± 0.052	2.650 ± 0.050	1.395 ± 0.061	$\lesssim$ 0.167

TABLE 4A—*Continued*

HD No. Type Name	f_X $f_{N\ V}$	f_{S1} $f_{O\ I}$	f_{S2} $f_{C\ II}$	$f_{C\ IV}$ $f_{Si\ IV}$	$f_{Mg\ II\ h}$ [$\Delta\lambda$ (Å)] $f_{He\ II}$
114613 G3 V	0.76 ± 0.24	...	...	$\lesssim$ 0.118	...
HR 4979	0.123 ± 0.040:	$\lesssim$ 0.012	$\lesssim$ 0.037	$\lesssim$ 0.060	0.134 ± 0.040:
32923 2×G4 V	$\lesssim$ 0.20	...	...	$\lesssim$ 0.041	...
104 Tau	$\lesssim$ 0.024	$\lesssim$ 0.020	0.019 ± 0.006	$\lesssim$ 0.037	$\lesssim$ 0.037
20630 G5 V	7.39 ± 0.41	28 ± 9	25 ± 21	0.375 ± 0.014	9.6 ± 1.5 [1.3]
κ^1 Cet	0.038 ± 0.005	0.169 ± 0.007	0.264 ± 0.018	0.292 ± 0.014	0.185 ± 0.010
115617 G5 V	$\lesssim$ 0.20	...	...	0.041 ± 0.011	2.7 ± 0.1 [1.3]
61 Vir	$\lesssim$ 0.022	$\lesssim$ 0.021	0.027 ± 0.006	$\lesssim$ 0.031	$\lesssim$ 0.028
117176 G5 V	$\lesssim$ 0.20	...	...	$\lesssim$ 0.060	...
70 Vir	$\lesssim$ 0.025	0.022 ± 0.006	$\lesssim$ 0.015	$\lesssim$ 0.031	$\lesssim$ 0.033
20794 G8 V	$\lesssim$ 0.20	...	...	0.082 ± 0.040:	4.3 ± 0.4 [1.3]
HR 1008	$\lesssim$ 0.034	0.100 ± 0.011	0.044 ± 0.015:	$\lesssim$ 0.053	0.095 ± 0.040:
10700 G8 V	0.31 ± 0.10	$\lesssim$ 12	$\lesssim$ 15	0.053 ± 0.009	8.1 ± 0.4 [1.3]
τ Cet	$\lesssim$ 0.024	0.119 ± 0.007	0.056 ± 0.008	0.075 ± 0.012	$\lesssim$ 0.026
131156 G8 V	16.00 ± 0.70	25 ± 5	48 ± 6	0.585 ± 0.007	15.4 ± 1.1 [1.3]
ξ Boo A	0.065 ± 0.006	0.296 ± 0.005	0.454 ± 0.007	0.340 ± 0.007	0.433 ± 0.012
166 K0 V	3.31 ± 0.34	$\lesssim$ 18	$\lesssim$ 18	0.158 ± 0.010	3.2 ± 0.1 [1.3]
HR 8	0.044 ± 0.007	0.071 ± 0.005	0.108 ± 0.005	0.150 ± 0.010	0.108 ± 0.009
185144 K0 V	1.12 ± 0.41	$\lesssim$ 5	$\lesssim$ 6	0.100 ± 0.013	...
σ Dra	$\lesssim$ 0.023	0.058 ± 0.007	0.089 ± 0.007	$\lesssim$ 0.030	0.040 ± 0.015:
165341 K0 V	10.20 ± 0.60	$\lesssim$ 36	43 ± 14	0.459 ± 0.017	17.4 ± 3.7 [1.3]
70 Oph	0.060 ± 0.007	0.356 ± 0.010	0.461 ± 0.015	0.210 ± 0.011	0.273 ± 0.010
155886,5 K0+K1V	4.15 ± 0.45	15 ± 8	20 ± 10	0.254 ± 0.025	9.9 ± 1.6 [1.3]
36 Oph AB	$\lesssim$ 0.060	0.239 ± 0.018	0.256 ± 0.046	0.136 ± 0.015	0.175 ± 0.018
26965 K1 V	0.88 ± 0.06[b]	14 ± 6[b]	16 ± 7[b]	0.065 ± 0.010	6.6 ± 3.6 [1.3]
o^2 Eri	$\lesssim$ 0.010	0.068 ± 0.005	0.070 ± 0.010	0.015 ± 0.005	0.030 ± 0.003
10476 K1 V	$\lesssim$ 0.20	...	...	0.017 ± 0.006:	...
107 Psc	$\lesssim$ 0.010	0.025 ± 0.002	0.025 ± 0.002	0.033 ± 0.010:	$\lesssim$ 0.004
17925 K1 V	6.5 ± 0.5	$\lesssim$ 36	$\lesssim$ 36	0.301 ± 0.006	3.7 ± 0.8 [1.3]
HR 857	0.070 ± 0.010:	0.106 ± 0.005	0.139 ± 0.007	0.170 ± 0.012	0.174 ± 0.009
128621 K1 V	13.60 ± 0.40[a]	123 ± 10[a]	248 ± 14[a]	1.400 ± 0.033	82 ± 9 [1.3]
α^2 Cen	0.142 ± 0.030:	1.250 ± 0.031	1.500 ± 0.058	0.683 ± 0.023	0.318 ± 0.026
22049 K2 V	17.20 ± 0.50	70 ± 15	63 ± 28	1.150 ± 0.025	28.0 ± 5.2 [1.3]
ϵ Eri	0.154 ± 0.006	0.595 ± 0.010	0.730 ± 0.017	0.444 ± 0.011	0.800 ± 0.021
16160 K3 V	0.30 ± 0.14	$\lesssim$ 36	$\lesssim$ 39	$\lesssim$ 0.051	1.5 ± 0.5 [1.3]
HR 753	$\lesssim$ 0.036	$\lesssim$ 0.017	$\lesssim$ 0.022	$\lesssim$ 0.044	$\lesssim$ 0.050
219134 K3 V	$\lesssim$ 0.20	...	...	0.075 ± 0.024	...
HR 8832	$\lesssim$ 0.043	$\lesssim$ 0.028	$\lesssim$ 0.080	$\lesssim$ 0.056	$\lesssim$ 0.056
209100 K4 V	2.21 ± 0.23	6 ± 4	7 ± 6	0.130 ± 0.023	7.8 ± 1.6 [1.3]
ϵ Ind	0.050 ± 0.020:	0.250 ± 0.028	0.130 ± 0.012	$\lesssim$ 0.059	0.085 ± 0.021
201091,2 K5+K7 V	2.33 ± 0.16	12 ± 4	8 ± 5	0.220 ± 0.040	7.2 ± 1.2 [1.3]
61 Cyg AB	$\lesssim$ 0.090	0.160 ± 0.020	0.150 ± 0.020	0.150 ± 0.040	0.200 ± 0.040

TABLE 4

B. *ROSAT* AND *IUE* FLUXES OF F5–K0 GIANTS

HD No. Type Name	f_X $f_{N\ V}$	f_{S1} $f_{O\ I}$	f_{S2} $f_{C\ II}$	$f_{C\ IV}$ $f_{Si\ IV}$	$f_{Mg\ II\ h}$ [Δλ (Å)] $f_{He\ II}$
71243 F5 III	1.20 ± 0.10	≲ 12	≲ 15	0.707 ± 0.067	···
α Cha	≲ 0.081	0.185 ± 0.025	0.432 ± 0.025	0.405 ± 0.047	≲ 0.220
1671 F5 III	0.44 ± 0.11	≲ 15	≲ 21	0.378 ± 0.012	7.4 ± 0.6 [2.3]
ρ And	≲ 0.022	0.174 ± 0.008	0.196 ± 0.008	0.200 ± 0.023	≲ 0.031
48737 F5 IV	3.00 ± 0.20	≲ 12	≲ 21	2.100 ± 0.150	···
ξ Gem	0.263 ± 0.046	0.773 ± 0.045	1.630 ± 0.051	1.133 ± 0.112	0.528 ± 0.150
61064 F6 III	0.39 ± 0.13	≲ 12	≲ 21	0.434 ± 0.041	7.1 ± 0.1 [2.0]
25 Mon	0.057 ± 0.018	0.185 ± 0.008	0.296 ± 0.020	0.280 ± 0.019	0.094 ± 0.031
35072 F7 III-IV	≲ 0.20	···	···	0.057 ± 0.013	1.0 ± 0.1 [1.3]
ζ Pic	≲ 0.013	≲ 0.021	≲ 0.029	0.071 ± 0.022	≲ 0.025
124850 F7 IV	5.6 ± 0.4	≲ 15	≲ 18	0.705 ± 0.050	13.3 ± 1.8 [1.3]
ι Vir	≲ 0.087	0.247 ± 0.016	0.506 ± 0.020	0.304 ± 0.031	≲ 0.168
220657 F8 III-IV	3.50 ± 0.30	≲ 27	≲ 27	1.680 ± 0.100	20.3 ± 1.7 [3.2]
υ Peg	0.168 ± 0.030:	0.584 ± 0.029	0.965 ± 0.072	0.702 ± 0.055	0.178 ± 0.050:
111812 G0 III	8.80 ± 0.20	9 ± 4	16 ± 6	1.810 ± 0.040	17.0 ± 1.0 [3.4]
31 Com	0.228 ± 0.020:	0.667 ± 0.017	0.808 ± 0.025	0.834 ± 0.022	0.371 ± 0.012
72779 G0 III	0.47 ± 0.15	≲ 18	≲ 36	0.360 ± 0.019	3.5 ± 0.4 [4.8]
35 Cnc	0.056 ± 0.007	0.157 ± 0.005	0.175 ± 0.007	0.169 ± 0.012	0.072 ± 0.013
6903 G0 III	0.24 ± 0.08	···	···	0.706 ± 0.013	9.0 ± 0.2 [4.8]
ψ^3 Psc	0.064 ± 0.008:	0.365 ± 0.008	0.296 ± 0.009	0.385 ± 0.012	0.139 ± 0.007
223460 G1 III	3.80 ± 0.50	≲ 18	≲ 24	0.350 ± 0.027	7.0 ± 0.3 [3.2]
HR 9024	0.350 ± 0.013	0.307 ± 0.009	0.127 ± 0.006	0.356 ± 0.013	0.352 ± 0.016
82210 G4 III-IV	16.60 ± 0.7	40 ± 5	39 ± 6	0.370 ± 0.027	18.4 ± 2.1 [1.5]
24 UMa	0.164 ± 0.015	0.500 ± 0.024	0.260 ± 0.019	0.419 ± 0.026	0.425 ± 0.020
141714 G4 III	3.58 ± 0.25	···	···	0.168 ± 0.013	10.3 ± 1.4 [1.8]
δ CrB	0.058 ± 0.014:	0.224 ± 0.013	0.093 ± 0.008	0.095 ± 0.010	0.121 ± 0.011
85444 G7 III	2.40 ± 0.20	14 ± 4	9 ± 6	0.220 ± 0.038	11.2 ± 1.1 [1.7]
υ^1 Hya	0.071 ± 0.020:	0.554 ± 0.021	0.141 ± 0.014	0.223 ± 0.019	0.160 ± 0.017
203387 G8 III	6.70 ± 0.40	12 ± 5	5 ± 5	≲ 0.287	10.9 ± 1.1 [2.3]
ι Cap	≲ 0.290:	0.437 ± 0.071	0.211 ± 0.050	≲ 0.242	≲ 0.220
115659 G8 III	1.50 ± 0.20	···	···	0.098 ± 0.008	11.1 ± 1.6 [2.2]
γ Hya	0.081 ± 0.010	0.372 ± 0.007	0.061 ± 0.016	0.125 ± 0.017	0.100 ± 0.020
150997 G8 III	0.28 ± 0.07	···	···	0.200 ± 0.015	11.6 ± 3.4 [1.8]
η Her	0.062 ± 0.020:	0.545 ± 0.010	0.125 ± 0.007	0.172 ± 0.014	0.130 ± 0.014
113226 G8 III	0.77 ± 0.14	···	···	0.085 ± 0.011	12.9 ± 2.6 [2.3]
ε Vir	0.072 ± 0.020:	0.308 ± 0.009	0.059 ± 0.006	0.084 ± 0.010	0.040 ± 0.010
28307 K0 III	4.96 ± 0.32	13 ± 6	6 ± 10	0.187 ± 0.015	9.4 ± 0.8 [1.8]
θ^1 Tau	0.090 ± 0.012:	0.391 ± 0.011	0.142 ± 0.006	0.165 ± 0.010	0.130 ± 0.008
27371 K0 III	2.10 ± 0.19	17 ± 5	9 ± 10	0.150 ± 0.009	8.8 ± 2.2 [1.8]
γ Tau	0.099 ± 0.010:	0.446 ± 0.007	0.095 ± 0.004	0.142 ± 0.008	0.096 ± 0.015
27697 K0 III	≲ 0.20	≲ 18	≲ 30	0.064 ± 0.018:	5.3 ± 0.8 [1.8]
δ^1 Tau	0.042 ± 0.014:	0.188 ± 0.009	0.050 ± 0.010	0.049 ± 0.010:	0.039 ± 0.012:
62509 K0 III	0.62 ± 0.13	≲ 12	≲ 12	0.271 ± 0.025:	50.0 ± 2.8 [1.8]
β Gem	0.090 ± 0.018:	1.330 ± 0.034	0.191 ± 0.009	0.313 ± 0.014	0.124 ± 0.030:
4128 K0 III	15.70 ± 0.60	26 ± 9	40 ± 10	0.629 ± 0.038	62.7 ± 4.5 [2.3]
β Cet	0.900 ± 0.039	3.390 ± 0.093	0.511 ± 0.027	0.964 ± 0.100	0.703 ± 0.029
28305 K0 III	0.12 ± 0.05	≲ 18	≲ 27	0.022 ± 0.005	5.4 ± 0.4 [1.8]
ε Tau	≲ 0.020:	0.169 ± 0.007	0.023 ± 0.004	0.056 ± 0.016:	≲ 0.018

TABLE 4

C. *ROSAT* AND *IUE* FLUXES OF MISCELLANEOUS TARGETS

HD No. Type Name	f_X $f_{N\ V}$	f_{S1} $f_{O\ I}$	f_{S2} $f_{C\ II}$	$f_{C\ IV}$ $f_{Si\ IV}$	$f_{Mg\ II\ h}$ [$\Delta\lambda$ (Å)] $f_{He\ II}$
61421 F5 IV	28.80 ± 0.70	81 ± 7	170 ± 10	10.400 ± 0.340	282 ± 28 [1.5]
α CMi	$\lesssim$ 0.586	5.270 ± 0.180	6.940 ± 0.220	4.540 ± 0.347	3.050 ± 0.680
121370 G0 IV	0.93 ± 0.19	$\lesssim$ 12	$\lesssim$ 18	0.309 ± 0.013	20.4 ± 1.6 [1.7]
η Boo	0.077 ± 0.025:	0.328 ± 0.025	0.319 ± 0.010	0.200 ± 0.028	$\lesssim$ 0.100
2151 G2 IV	0.94 ± 0.31	$\lesssim$ 27	$\lesssim$ 33	0.222 ± 0.021	11.6 ± 2.6 [1.3]
β Hyi	$\lesssim$ 0.030	0.216 ± 0.018	0.138 ± 0.013	0.099 ± 0.013	$\lesssim$ 0.060
190248 G7 IV	1.30 ± 0.45	$\lesssim$ 42	$\lesssim$ 42	0.150 ± 0.030	6.3 ± 1.2 [1.3]
δ Pav	$\lesssim$ 0.020:	0.091 ± 0.007	0.090 ± 0.019	0.120 ± 0.028	$\lesssim$ 0.010
34029b[c] G0 III	59.0 ± 1.00	382 ± 16	484 ± 19	45.900 ± 1.200	573 ± 46 [3.2]
α Aur Ab	5.800 ± 0.400	27.300 ± 0.700	24.500 ± 0.800	21.400 ± 0.800	6.900 ± 0.400
93497 G5 III	11.40 ± 1.80	24 ± 6	46 ± 8	1.150 ± 0.083	40 ± 6 [1.8]
μ Vel	0.383 ± 0.054	2.020 ± 0.078	0.676 ± 0.034	0.950 ± 0.086	0.420 ± 0.047
34029a[c] G8 III	59.0 ± 1.00	382 ± 16	484 ± 19	4.600 ± 0.100	171 ± 14 [3.2]
α Aur Aa	1.200 ± 0.300:	7.600 ± 0.200	1.230 ± 0.040	3.200 ± 0.100	1.900 ± 0.100
36079 G5 II	$\lesssim$ 0.20	...	...	$\lesssim$ 0.042	13.3 ± 0.6 [1.8]
β Lep	0.053 ± 0.020:	0.279 ± 0.008	0.023 ± 0.006	0.043 ± 0.011	$\lesssim$ 0.041
109379 G5 II	$\lesssim$ 0.20	...	...	0.152 ± 0.023	15.3 ± 1.2 [2.2]
β Crv	$\lesssim$ 0.049	0.520 ± 0.009	0.081 ± 0.006	0.172 ± 0.023	0.076 ± 0.020
31910 G1 Ib-II	0.39 ± 0.13	$\lesssim$ 12	$\lesssim$ 18	0.514 ± 0.024	18.4 ± 0.2 [4.0]
β Cam	0.400 ± 0.040:	1.500 ± 0.000	0.213 ± 0.010	0.450 ± 0.026	0.200 ± 0.030
159181 G2 Iab:	1.50 ± 0.10	$\lesssim$ 12	$\lesssim$ 12	2.680 ± 0.049	82 ± 6 [3.9]
β Dra	0.849 ± 0.030	5.390 ± 0.120	1.070 ± 0.026	1.720 ± 0.037	0.672 ± 0.025

TABLE 4

D. *ROSAT* AND *IUE* FLUXES OF HYBRID CHROMOSPHERE STARS

HD No. Type Name	f_X $f_{N\ V}$	f_{S1} $f_{O\ I}$	f_{S2} $f_{C\ II}$	$f_{C\ IV}$ $f_{Si\ IV}$	$f_{Mg\ II\ h}$ [$\Delta\lambda$ (Å)] $f_{He\ II}$
124897 K1 III	$\lesssim$ 0.002[d]	...	...	0.284 ± 0.060:	254 ± 30 [2.3]
α Boo	$\lesssim$ 0.150	14.500 ± 0.300	0.499 ± 0.050:	$\lesssim$ 0.200	0.915 ± 0.051
81817 K3 III	$\lesssim$ 0.20[e]	...	...	0.060 ± 0.020	3.4 ± 0.6 [3.2]
HR 3751	$\lesssim$ 0.025	0.417 ± 0.012	0.039 ± 0.010:	0.044 ± 0.012:	0.033 ± 0.008:
198700 K1 II	0.07 ± 0.01[f]	...	...	0.125 ± 0.012	10.9 ± 2.2 [3.2]
β Ind	0.140 ± 0.025:	0.781 ± 0.066	0.062 ± 0.006	0.182 ± 0.021	0.048 ± 0.010
163770 K1 IIa	$\lesssim$ 0.20[e]	...	...	0.069 ± 0.005	8.0 ± 1.8 [3.5]
θ Her	0.061 ± 0.010:	1.060 ± 0.052	0.029 ± 0.003	0.083 ± 0.006	0.090 ± 0.004
150798 K2 II-III	0.75 ± 0.28[e,g]	...	...	0.561 ± 0.031	51 ± 4 [3.5]
α TrA	0.343 ± 0.046	5.360 ± 0.550	0.213 ± 0.010	0.280 ± 0.033	0.541 ± 0.014
186791 K3 II	0.008 ± 0.003[f]	...	...	0.112 ± 0.007	18.8 ± 3.2 [3.5]
γ Aql	0.113 ± 0.040:	2.000 ± 0.087	0.076 ± 0.013	$\lesssim$ 0.060	0.180 ± 0.006
31398 K3 II	$\lesssim$ 0.004[f,h]	...	...	0.072 ± 0.010:	15.0 ± 2.2 [3.2]
ι Aur	0.080 ± 0.014	1.420 ± 0.079	0.049 ± 0.008	0.060 ± 0.016:	0.113 ± 0.006
204867 G0 I	$\lesssim$ 0.20[e]	...	...	0.315 ± 0.015	29 ± 4 [3.9]
β Aqr	0.150 ± 0.040:	1.900 ± 0.055	0.129 ± 0.011	0.272 ± 0.032	0.123 ± 0.011
209750 G2 Ib	$\lesssim$ 0.20[e]	...	...	0.449 ± 0.018	36 ± 4 [4.0]
α Aqr	0.201 ± 0.022	2.900 ± 0.079	0.221 ± 0.007	0.506 ± 0.024	0.206 ± 0.023
145544 G2 Ib-II	$\lesssim$ 0.20[e]	...	...	0.234 ± 0.030:	14.4 ± 2.0 [4.0]
δ TrA	0.088 ± 0.025:	1.500 ± 0.041	0.084 ± 0.008	0.156 ± 0.018	0.107 ± 0.018

TABLE 4

E. *ROSAT* AND *IUE* FLUXES OF RS CVn BINARIES

HD No. Type Name	f_X $f_{N\ V}$	f_{S1} $f_{O\ I}$	f_{S2} $f_{C\ II}$	$f_{C\ IV}$ $f_{Si\ IV}$	$f_{Mg\ II\ h}$ [$\Delta\lambda$ (Å)] $f_{He\ II}$
108102 2xF8 V	4.50 ± 0.30	16 ± 4	$\lesssim$ 18	0.222 ± 0.008	1.1 ± 0.1 [2.2]
IL Com	0.040 ± 0.011	0.028 ± 0.004	0.095 ± 0.005	0.094 ± 0.008	0.081 ± 0.008:
77137 2xG5 IV	13.40 ± 0.70	28 ± 5	34 ± 8	0.607 ± 0.014	3.9 ± 0.4 [3.9]
TY Pyx	0.105 ± 0.006:	0.133 ± 0.005	0.341 ± 0.010	0.206 ± 0.007	0.181 ± 0.006
106677 2xK0 III	9.30 ± 0.60	...	...	0.655 ± 0.030	9.5 ± 1.0 [3.2]
DK Dra	0.277 ± 0.025:	0.653 ± 0.016	0.280 ± 0.010	0.325 ± 0.014	0.295 ± 0.014

NOTES TO TABLE 4.—Fluxes and 1σ uncertainties (or 3σ upper limits) in 10^{-12} ergs cm^{-2} s^{-1} at Earth, except for *ROSAT* WFC S1 and S2 which are in counts per kilosecond. No corrections for interstellar reddening have been applied. For *ROSAT* PSPC survey detections, a uniform energy conversion factor 5.5×10^{-12} ergs cm^{-2} count^{-1} was used. Colons indicate that values were modified (usually, $\sigma_{new} = 2 \times \sigma_{old}$) based on examination of automated fits. Some fluxes were not measured: on the *ROSAT*/WFC side, because the star was faint in f_X or at large N_H; on the *IUE* side, because suitable SWP-LO or LW-HI images were not available from the NSSDC. See text for discussion of σ_{MgIIh}.

[a] *ROSAT* X-ray flux divided 28% to G star and 72% to K star based on EXO/HRI; WFC EUV fluxes not adjusted.

[b] *ROSAT* X-ray flux divided 22% to K star based on EXO/HRI [78% to M star]; WFC EUV fluxes not adjusted: probably mostly from WD.

[c] *ROSAT* X-ray flux divided 50% to G8 star and 50% to G0 star based on Ayres, Schiffer, & Linsky 1983; WFC EUV fluxes not adjusted; *IUE* FUV and Mg II *h* fluxes divided according to Ayres 1988.

[d] Upper limit from 19 ks PSPC pointing of Ayres, Fleming, & Schmitt 1991.

[e] PSPC survey fluxes and upper limits from Haisch, Schmitt, & Rosso, 1992.

[f] Fluxes and upper limits from 5–11 ks PSPC pointings of Reimers & Schmitt 1992.

[g] $f_X = 0.51 \pm 0.04$ (quiescent) from 32 ks PSPC pointing of Kashyap et al. 1994.

[h] $f_X = 0.0044 \pm 0.0011$ from 26 ks PSPC pointing of Kashyap et al. 1994.

IV, and less than 10% in Mg II *h*. Such deviations can be significant with respect to the measurement errors (typically $\gtrsim$ 5% and $\gtrsim$ 3%, respectively) in a given time sequence. However, when considering the statistical activity levels of broad samples of stars, such deviations are completely unimportant. Thus, we confidently can compare the RASS X-ray fluxes to noncontemporaneous *IUE* spectra.

5.2. *Flux-Flux Diagrams*

One of the main purposes of the present work is to update the flux-flux correlation diagrams presented more than a decade ago by AML. The "correlograms" provide an intriguing perspective on the relationships among chromosphere, corona, and the intervening transition zone (TZ: $T \approx 10^5$ K). AML showed that coronal X-rays rose steeply with increasing Mg II with a power-law slope of $\approx$ 3, when both were normalized to the stellar bolometric fluxes. In addition, a TZ flux composed of Si IV + C IV + N V increased with a power-law slope of $\approx$ 1.5 when compared with chromospheric Mg II.

The nonlinear power laws are difficult to reconcile with a straightforward "solar analog" that explains enhanced emissions of MS stars through increased surface coverage by some fundamental quantum of magnetic activity. In that picture, the flux-flux relations would have power-law slopes of unity up to the point where the surface filling by the active quanta was complete. Invoking a "basal" (fixed lower bound) flux in the Mg II emissions does flatten the X-ray–Mg II relation somewhat (Schrijver 1987). It offers little help with the coronal versus TZ emissions, however, where any lower limit to the C IV flux must be quite small (e.g., α Boo).

Concerns have been raised in the past, however, with regard to comparisons of X-ray fluxes from different instruments (e.g., *HEAO* 1, *Einstein,* and *EXOSAT*) with *IUE UV* fluxes obtained in different epochs, measured by different workers using different techniques. Now we have a uniform set of fluxes for which the question of temporal variations has been addressed quantitatively (and dismissed). Figures 13–16 illustrate representative correlation diagrams. In each we separated the stars by luminosity class and spectral type. We fitted power laws through the solar and cooler dwarfs (collectively and in subsets), and repeated the MS relations in the other panels. Table 6 summarizes the inferred slopes.

In the X-ray versus *UV* diagrams we included 3 σ X-ray upper limits for the former but not the latter. The *IUE* measurements do not have as uniform a sensitivity threshold as the PSPC survey. In the C IV versus Mg II and PSPC versus WFC diagrams we plotted only the detections. The uppermost point in each panel usually is an RS CVn. The lowest X-ray point belongs to α Boo, a denizen of the coronal graveyard.

In Figure 13 the MS stars occupy a broad band of normalized X-ray and C IV emissions. The range is three orders of magnitude in the former, and two in the latter. The G/K dwarfs obey a tight relation with an overall power-law slope of $\approx$1.5. A few of the mid-F stars trail off toward depressed X-ray emission (as SD found for the early-F stars). Curiously, the power law for the F9-G2 "solar-type" dwarfs is significantly steeper than that for the G8–K5 MS stars.

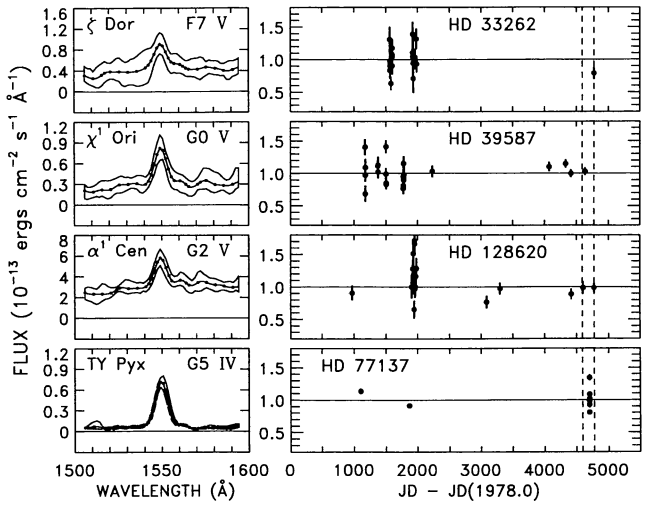

FIG. 11*a*

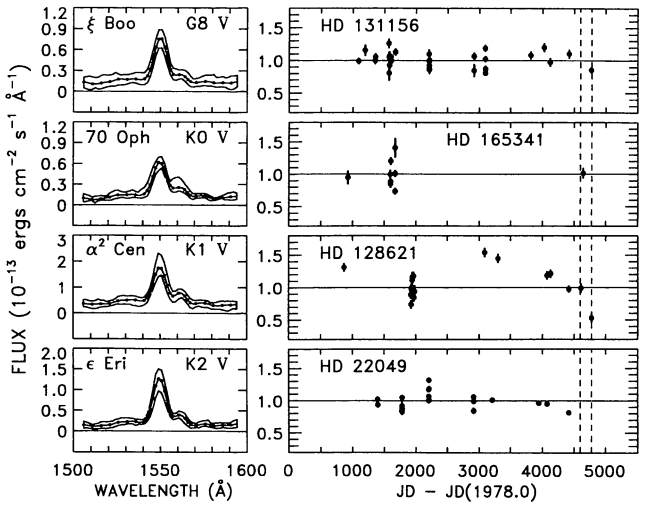

FIG. 11*b*

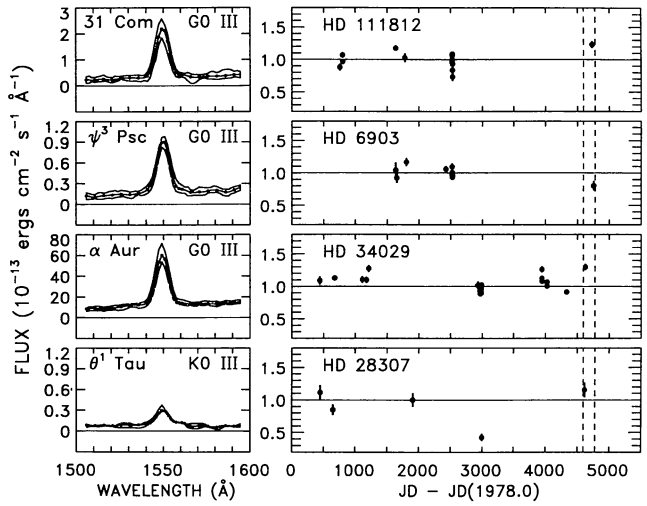

FIG. 11*c*

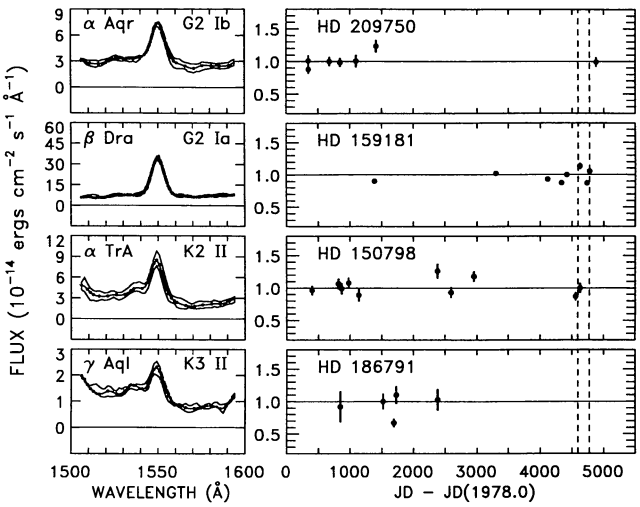

FIG. 11*d*

FIG. 11.—(*a*) C IV time series for F/G dwarfs (and the RS CVn binary TY Pyx). The left-hand panels show the average SWP-LO profile (*dots*). The thin curves are the extreme excursions (after application of an "Olympic" filter: see text). The right-hand panels illustrate the long-term behavior of C IV, relative to the median value of the series. The RIASS epoch is indicated by vertical dashed lines. (*b*) Same as (*a*) for G/K dwarfs. (*c*) Same as (*a*) for G/K giants. (*d*) Same as (*a*) for G/K supergiants.

The subgiants, although sparsely represented, mostly behave like the dwarf stars. A few of the hotter members appear to be X-ray deficient. The normal giants occupy a broader range of coronal and TZ emissions than the MS stars even ignoring the remarkably small upper limit on the X-ray flux of α Boo. Here the dichotomy between the warmer and cooler giants is more pronounced than that between the mid-F and later dwarfs in Figure 13*a*. The cooler giants, like their MS counterparts, show a flatter power-law (slope ≈ 1) than the F9–G2 dwarfs. However, the Hertzsprung gap giants fall below the MS curves, and their X-ray deficiency can be an order of magnitude or more (SD). Among the supergiants virtually all of the firmly detected objects are X-ray deficient, although the archetype hybrid α TrA lies only slightly below the MS trend.

Figure 14 paints essentially the same picture in Mg II *h*. Few if any dwarfs are X-ray deficient. Among the more luminous objects, however, X-ray deficient stars appear, and the phenomenon advances to cooler spectral types. There also is evidence for a basal level of $\mathscr{R}_h \approx 4 \times 10^{-6}$, at least in the giants and supergiants.

Figure 15 demonstrates that C IV is well correlated with Mg II *h* in essentially all of the stars. The power-law slopes differ between the solar and G8–K5 dwarfs at the 1.5 σ level. The supergiants show a slight but systematic under luminosity in C IV compared with Mg II *h*. It is remarkable that such a diversity of MK types and luminosity classes can exhibit so uniform a behavior in a diagram comparing TZ and chromospheric properties. It not only emphasizes the utility of the normalized

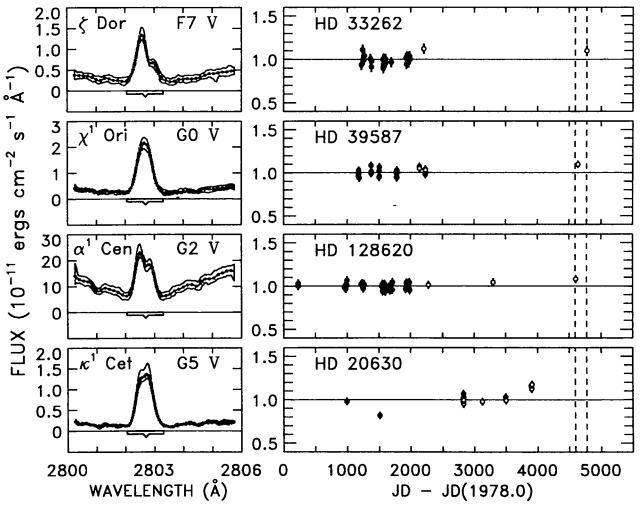

FIG. 12*a*

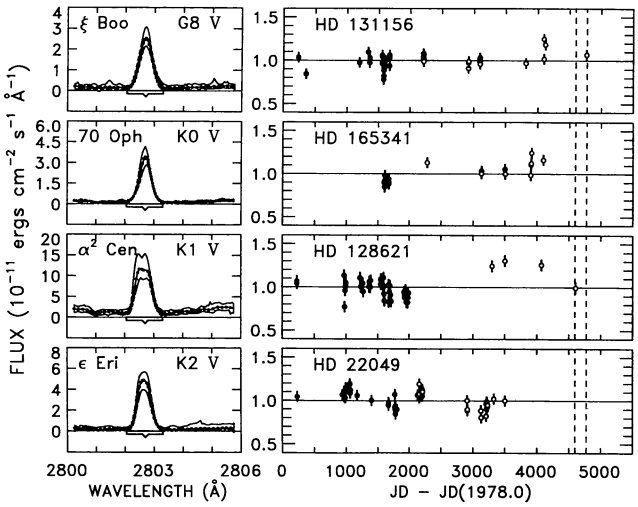

FIG. 12*b*

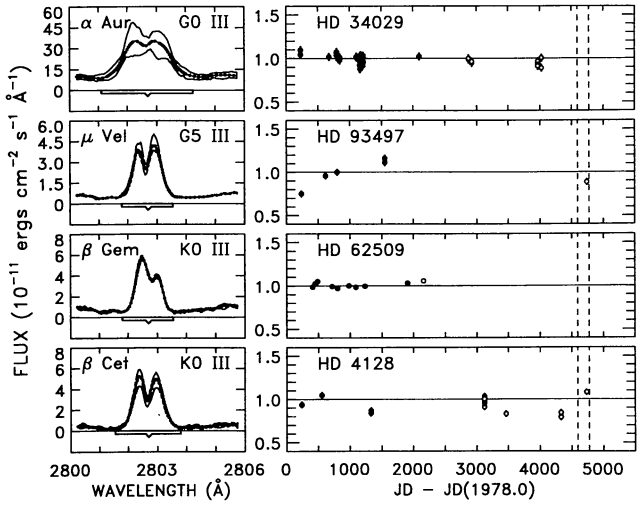

FIG. 12*c*

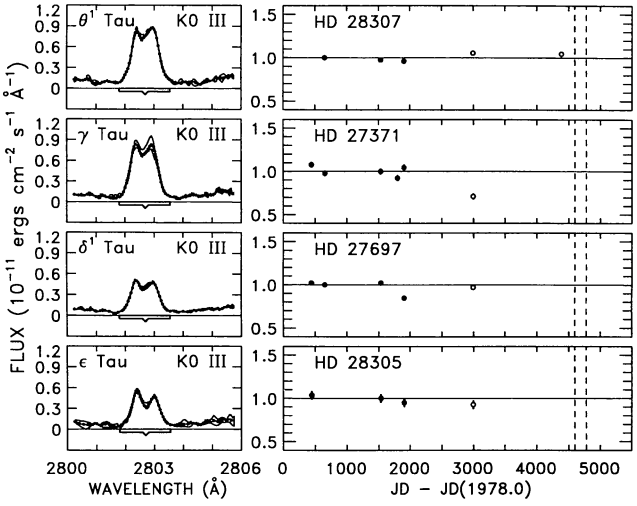

FIG. 12*d*

FIG. 12.—(*a*) Mg II *h* time series for F/G dwarfs. In the left-hand panel, the mean and extreme profiles (after Olympic filtering) are illustrated in the same way as those of Figs. 11. The bar under the profile depicts the adopted integration bandpass. In the right-hand panel, solid and open dots designate LWR and LWP, respectively. (*b*) Same as (*a*) for G/K dwarfs. (*c*) Same as (*a*) for G/K giants. (*d*) Same as (*a*) for the Hyades K giants. (*e*) Same as (*a*) for K-type hybrids. (*f*) Same as (*a*) for G-type supergiants. (*g*) Same as (*a*) for additional interesting objects.

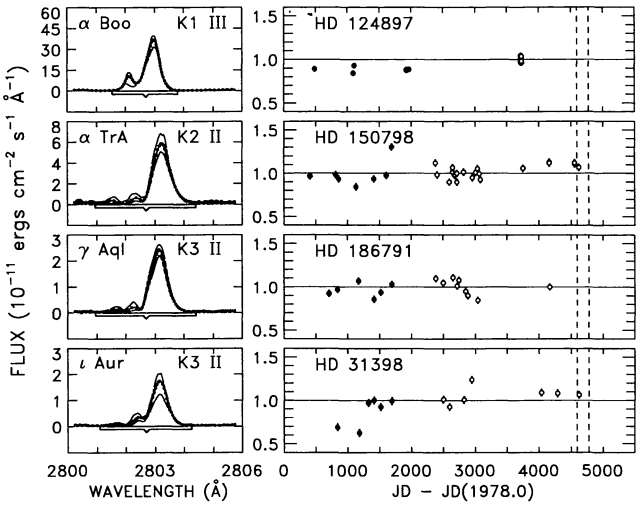

FIG. 12*e*

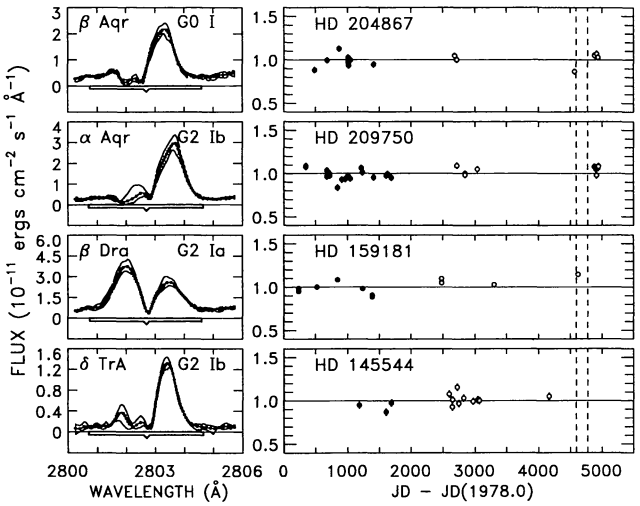

FIG. 12*f*

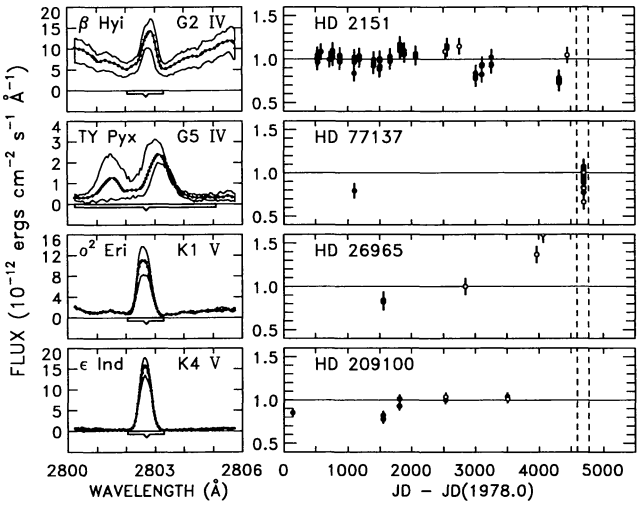

FIG. 12*g*

fluxes, but also abets the suspicion that the heating of the neighboring plasma regimes is accomplished by a single mechanism, presumably magnetic.

Figure 16 shows that the PSPC X-ray fluxes are well correlated with the WFC fluxes of the dwarf stars in both the S1 and S2 filters with a power-law slope of 1.2–1.4. A shallow slope is expected since the 65–195 Å interval is dominated by high-excitation emissions. Unfortunately the more luminous stars of the sample are too absorbed to be detected by the WFC. No obvious large inconsistencies appear between the X-rays and the absorption-sensitive EUV fluxes of the F dwarfs or the (few) Hertzsprung gap giants. That would seem to eliminate any explanation of the X-ray deficiency in terms of local absorption (cf., Haisch, Schmitt, & Fabian [1992] for the K giants redward of the LH dividing line).

5.3. *Flux-Ratio Diagrams*

Figures 17–19 depict X-rays or C IV plotted against ratios of two diagnostics. We included only ratios significant at the ≥5 σ level. Again we established an approximate power-law relationship for the MS stars and repeated it for the higher luminosities.

Figure 17 compares N V/C IV and Si IV/C IV with coronal activity. In a collisionally controlled equilibrium plasma Si IV forms at 6×10^4 K, C IV at 1×10^5 K, and N V at 2×10^5 K. High-resolution solar spectra (e.g., Kurucz 1991) and *HST*/GHRS G140L spectra of the K giant γ Dra (Linsky, Brown, & Carpenter 1991) indicate that the FUV features are not contaminated at SWP-LO resolution by extraneous emissions like Fe II or Si I.

The flux-flux relations steepen relatively slowly with decreasing formation temperature (e.g., from X-rays to C IV to Mg II). Thus one expects the ratios of the neighboring excitation stages to be nearly independent of activity. However, N V is significantly enhanced with respect to C IV among the cooler giants and supergiants compared to the MS trend. In contrast, the few Hertzsprung gap giants have more nearly the MS ratio. The Si IV emission also shows a slight enhancement relative to C IV among the Clump giants, but again the MS ratio for the Hertzsprung gap giants.

Optical work has revealed that postflash giants can display significant photospheric enhancements of nitrogen and slight depletions of carbon (e.g., Luck 1978; Lambert & Ries 1981; Luck & Lambert 1981). CNO-processed material from the interior is thought to be mixed to the surface during "first dredge-up" at the base of the giant branch. Böhm-Vitense & Mena-Werth (1992) previously proposed that the N V/C IV ratio could be employed as an abundance tracer. We confirm their conclusion, however, that some of the N V/C IV ratios are unusually large compared with dredge-up models. Thus, other selective enhancement mechanisms might be operating as well.

Figure 18 compares C IV/C II and O I/Mg II *h* with coronal activity. The C II emission forms at $\sim 3 \times 10^4$ K. The C IV/C II ratio exhibits a slight tilt toward higher activity among the MS stars, as expected from the nonlinear flux-flux relations. The ordinary giants and supergiants of all categories show a nearly vertical relation, indicating that C II behaves more like higher excitation C IV in such stars. That is a somewhat coun-

TABLE 5

LONG-TERM VARIABILITY

HD Number	Name	Type	C IV λ1549 rms (%)	C IV λ1549 <σ>[N] (%)	Mg II λ2802 rms (%)	Mg II λ2802 <σ>[N] (%)
			Dwarfs			
33262	ζ Dor	F7 V	18.5	16.0 [21]	5.2	5.7 [35]
39587	χ^1 Ori	G0 V	17.3	9.8 [24]	4.3	4.2 [29]
128620	α^1 Cen	G2 V	25.2	12.1 [18]	3.4	4.6 [51]
20630	κ^1 Cet	G5 V	...	...	7.8	4.2 [18]
131156	ξ Boo A	G8 V	11.8	6.0 [34]	7.9	5.8 [46]
165341	70 Oph	[K0 V]	18.5	7.3 [09]	10.7	6.1 [20]
26965	o^2 Eri	K1 V	...	...	27.3	8.6 [05]
128621	α^2 Cen	K1 V	22.2	6.5 [20]	11.0	6.6 [51]
22049	ε Eri	K2 V	12.7	4.2 [20]	9.4	6.1 [65]
209100	ε Ind	K4 V	...	...	10.1	5.0 [09]
			Subgiants			
2151	β Hyi	G2 IV	...	...	7.2	8.9 [64]
77137	TY Pyx	[G5 IV]	14.2	3.7 [09]	10.8	9.0 [27]
			Giants			
34029	α Aur A	[G0 III]	10.6	2.7 [33]	4.0	4.4 [77]
111812	31 Com	G0 III	12.0	5.0 [16]	...	...
6903	ψ^3 Psc	G0 III	8.9	5.8 [12]	...	...
93497	μ Vel	G5 III	...	...	14.0	3.8 [06]
28307	θ^1 Tau	K0 III	29.0	10.0 [05]	3.7	2.4 [05]
27371	γ Tau	K0 III	...	...	12.5	3.4 [06]
27697	δ^1 Tau	K0 III	...	...	6.7	2.3 [05]
62509	β Gem	K0 III	...	...	2.8	2.6 [10]
4128	β Cet	K0 III	...	...	8.0	3.7 [30]
124897	α Boo	K1 III	...	...	6.0	3.1 [25]
			Supergiants			
204867	β Aqr	G0 I	...	...	7.0	3.4 [14]
209750	α Aqr	G2 Ib	9.8	7.7 [07]	6.0	3.4 [29]
159181	β Dra	G2 Iab:	9.0	3.5 [08]	7.7	2.7 [13]
145544	δ TrA	G2 Ib-II	...	...	6.8	3.9 [13]
150798	α TrA	K2 II-III	11.6	8.0 [10]	9.1	4.0 [28]
186791	γ Aql	K3 II	15.7	15.2 [05]	8.3	3.9 [15]
31398	ι Aur	K3 II	...	...	16.0	4.5 [13]

terintuitive result, because the C II lines can become optically thick in giant stars, and their formation can be driven to cooler temperatures by Lyα photoionization of chromospheric atomic carbon (e.g., Judge 1986). Böhm-Vitense & Mena-Werth (1991) suggested that there is a separation in C IV/C II ratios between the warmer and cooler giants, possibly in response to a change in the TZ heating mechanism (cf., SD). Our ratios show no evidence for such a separation. The enhancement of O I with respect to Mg II in the evolved stars compared with the MS trend very likely is due to Bowen fluorescence (H I Lyβ pumping) as discussed by Haisch et al. (1977), and more recently by Carlsson & Judge (1993).

Figure 19 illustrates ratios of X-rays to He II λ1640 and He II/Si IV as functions of $\mathscr{R}_{\rm C\,IV}$. He II Baα is a coronal proxy, because it is produced partly by a photoionization/recombination process driven by EUV radiation (e.g., Hartmann et al. 1979). While the importance of recombination has been challenged in the empirical solar work of Athay (1988), it has been reinforced in the recent theoretical study by Wahlstrøm & Carlsson (1994). Here, the MS stars exhibit essentially a 1:1 correlation between X-rays and He II as a function of increasing activity, as expected under the recombination hypothesis. At the same time, however, He II shows a nearly 1:1 correlation with Si IV, a species that forms near the collisional ionization equilibrium temperature of He II and is not affected by possible abundance anomalies. Ordinarily, that behavior could be taken as support for the collisional hypothesis, except that the empirical relation is dominated by the cooler dwarfs which also show a nearly 1:1 correlation between their coronal and TZ emissions. The behavior of the cooler giants is consistent with that of the cooler dwarfs in both ratios, while the warmer giants fall on a significantly tilted X-ray/He II relation.

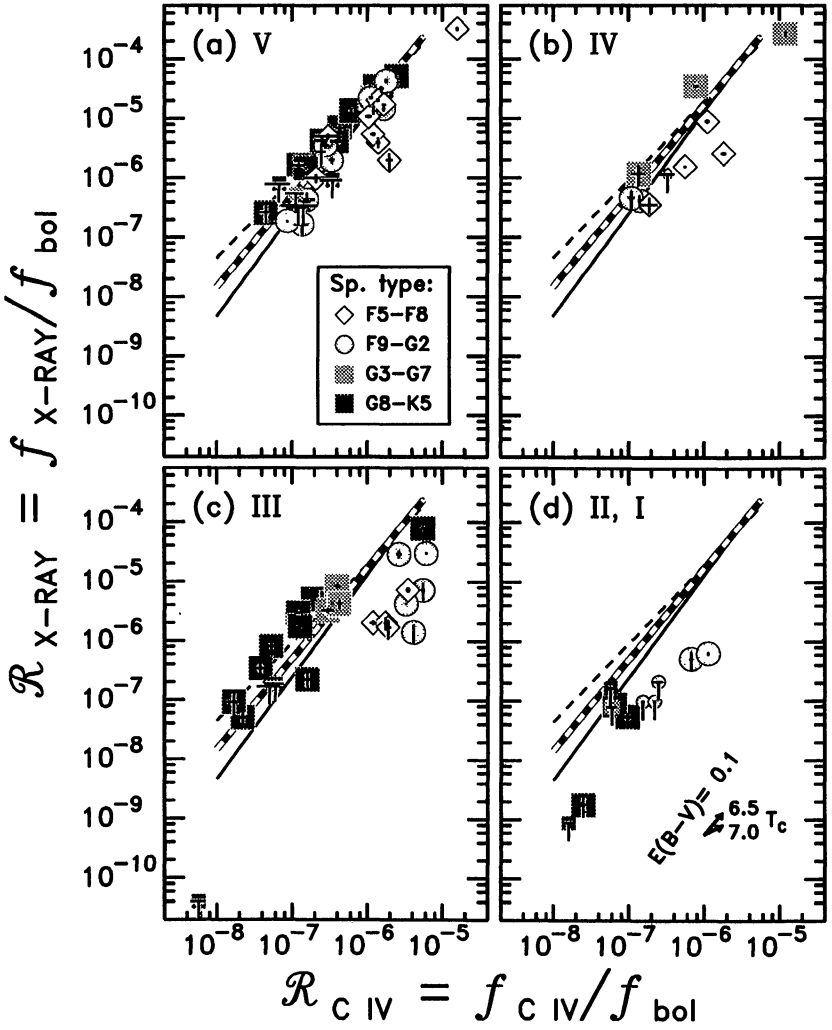

FIG. 13

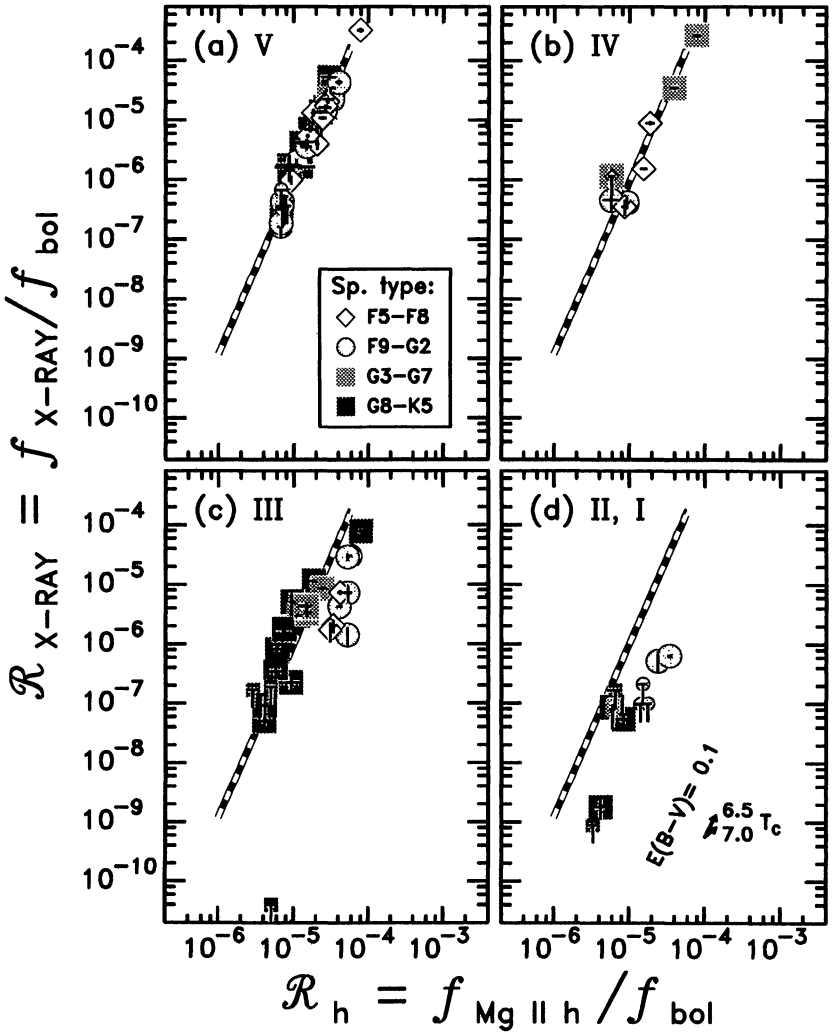

FIG. 14

FIG. 13.—(*a–d*) Flux-flux correlation diagram: X-rays vs. C IV. The stellar emissions have been normalized to the bolometric fluxes to permit fair comparisons among the diverse luminosities. The stars are separated according to MK luminosity class, and color/symbol coded into four spectral type intervals within each panel. Smaller symbols indicate 3 σ upper limits (X-rays, only). The thick dashed line is a power-law fit to the F9–K5 MS stars. The thin solid line was derived for the F9-G2 "solar-type" dwarfs, and the thin dashed line for the cooler G8–K5 dwarfs. The MS power laws are repeated in the other panels for comparison. Here, the main X-ray/C IV power law has slope 1.5. The legend in (*d*) illustrates how a point would move if dereddened for $E(B-V) = 0.^{m}1$ according to the X-ray attenuation described by Haisch, Schmitt, & Fabian (1992) and the average galactic UV extinction curve of Savage & Mathis (1979).

FIG. 14.—(*a–d*) X-rays vs. Mg II *h*. The main power law has a slope of 2.9 (cf., AML).

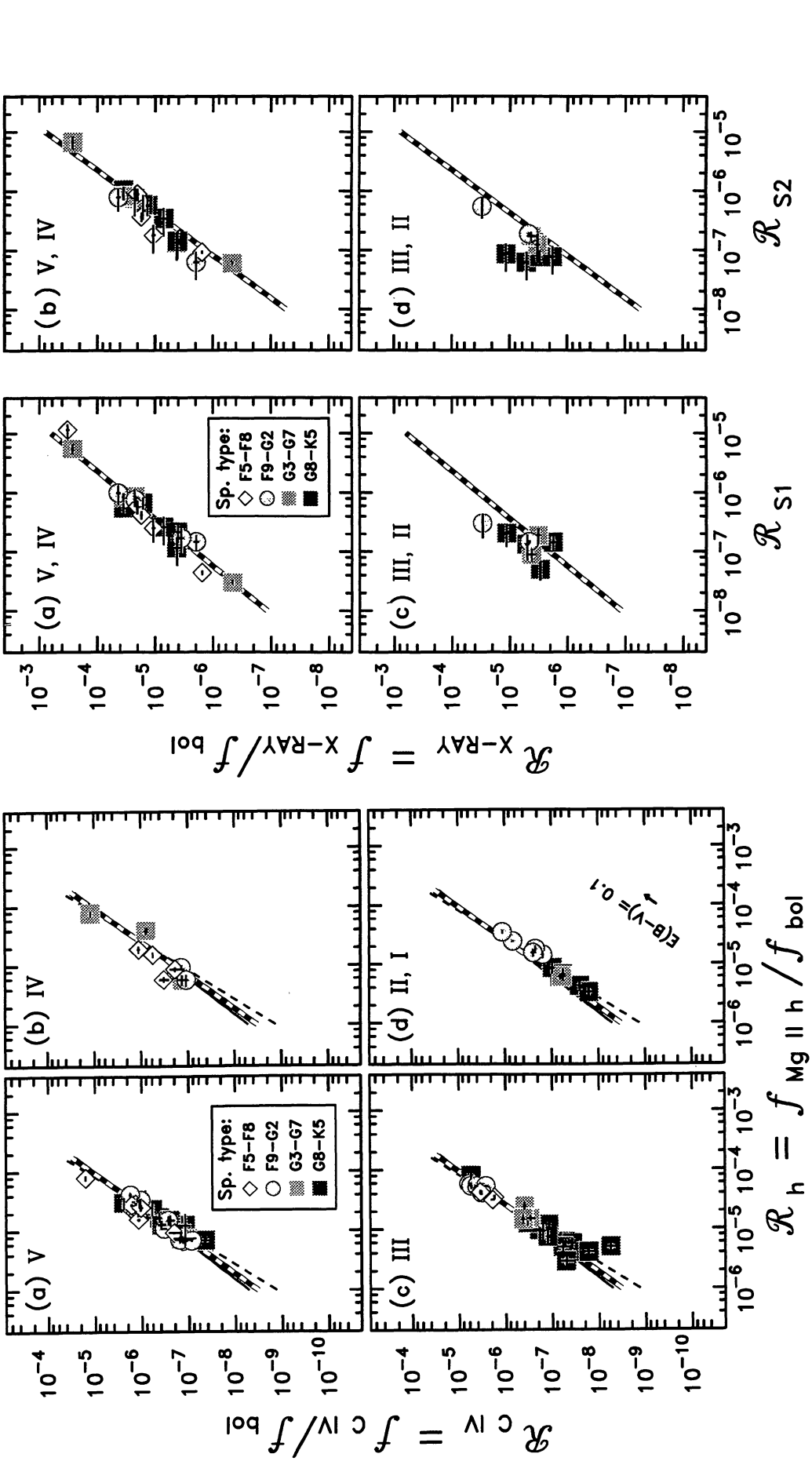

FIG. 15.—(*a–d*) C IV vs. Mg II *h*. The main power law has a slope of 1.8.

FIG. 16

FIG. 16.—X-rays vs. WFC. The abscissa scales are based on an (unphysical) ECF of 1×10^{-11}. The true conversion factors are highly dependent on (mostly) unknown hydrogen columns and source temperatures. Nevertheless, the scales should be approximately valid in a relative sense. The power-law slopes are (*a,c*) 1.2 (S1) and (*b,d*) 1.4 (S2). They were fitted to the near-MS (V, IV) F9–K5 stars. Only firm detections were used. The luminosity classes are divided more coarsely than in the previous diagrams.

TABLE 6

POWER-LAW SLOPES

Diagnostics	Spectral Types	Slope $\pm 1\sigma$
X-rays vs. C IV	F9–K5 V	1.53 ± 0.06
	F9–G2 V	1.72 ± 0.10
	G8–K5 V	1.32 ± 0.09
X-rays vs. Mg II *h*	F9–K5 V	2.91 ± 0.13
	F9–G2 V	2.85 ± 0.17
	G8–K5 V	2.93 ± 0.23
C IV vs. Mg II *h*	F9–K5 V	1.77 ± 0.12
	F9–G2 V	1.64 ± 0.16
	G8–K5 V	2.03 ± 0.21
X-rays vs. WFC S1	F9–K5 V, IV	1.24 ± 0.12
X-rays vs. WFC S2	F9–K5 V, IV	1.38 ± 0.13

At the same time, the warmer giants display a nearly 1:1 correlation between He II and Si IV, although it is significantly displaced (factor of 2) below the MS trend. The somewhat contrary behavior of the warmer giants might signal a shift in formation mechanism, a possibility that could be explored with detailed modeling like that of Wahlstrøm & Carlsson (1994).

5.4. *The X-Ray Deficiency Syndrome*

One of the major departures of the present work from the exploratory study by AML is the "X-ray deficiency," reported originally by SD for the early-F dwarfs and the Hertzsprung gap giants. Here, we find that the effect is genuine and is not due, say, to the limited energy response of previous X-ray instruments. It extends beyond the two aforementioned classes, affecting virtually all of the bright giants and supergiants.

The C IV versus Mg II flux-flux diagrams, and possibly also the C IV versus He II/Si IV flux-ratio diagrams, suggest that the deficiency is on the X-ray side. It is not likely due to an anomalous emission measure in the 10^5 K layers. The X-ray deficiency reduces the contrast between the coronal emissions of the Hertzsprung gap giants and the most active of their more evolved cousins in the Clump. At the same time, it enhances the contrast between the brightest of the Clump coronae and those of the mid-K giants and supergiants, strengthening the impression of a sharp X-ray boundary beyond K0.

SD suggested that the X-ray deficient stars are distinguished from the "normal" solar-like behavior by a fundamental difference in coronal heating mechanisms. The authors proposed acoustic waves for the former, and a magnetic agency for the latter. SD further suggested that the coronae of the X-ray deficient stars are controlled by massive winds. These suddenly brake the fast stellar rotation near G0 when the heating reverts from acoustic to magnetic.

There is no doubt that the coronal heating undergoes a major alteration among the X-ray deficient stars. Nevertheless, their lower atmospheres traced by C IV and Mg II appear to be completely normal with regard to the flux-flux relations of MS stars as well as Clump giants. We find it suspicious that the heating mechanism could switch between two such different energy deposition schemes and leave the relationship between TZ and chromosphere untouched.

Among the X-ray deficient G-type supergiants there is a wide disparity in Mg II and C IV emissions between the active objects (β Cam, β Dra) and the quieter hybrid stars (α Aqr, β Aqr, and δ TrA). As mentioned previously, these supergiants are virtually identical to one another in terms of fundamental stellar parameters. The acoustic hypothesis dictates that stars of similar temperature and gravity should experience similar mechanical heating. β Ind and γ Aql show a comparable disparity among the cooler hybrids. The Hertzsprung gap giants are mixed in their behavior. The warmer F stars are relatively clumped in the X-ray/C IV flux-flux diagram, while the cooler stars near the G0 break are more diverse. Possibly there are different X-ray deficiency syndromes for the F-type stars, and the G0 giants and G/K supergiants.

A possible unifying characteristic among the Hertzsprung gap and the G/K supergiants is *coronal outflow*. For example, Capella shows a significant variability of the blue peak of its H I Lyα emission (Ayres et al. 1993). The most natural explanation invokes a moderate-speed wind (-200 km s^{-1}) of moderate excitation ($T \approx 10^5$ K) from the G0 secondary. Although the inferred mass-loss rate is not large, it is sufficient to drain away substantial amounts of energy and angular momentum. The archetype hybrid α TrA also shows evidence for a moderate velocity (-400 km s^{-1}), possibly coronal temperature, outflow (Ayres & Kashyap 1994), in addition to the lower speed (-80 km s^{-1}) low-excitation wind seen in the Mg II lines (Hartmann, Dupree, & Raymond 1981). The mass-loss rate of the hot wind might greatly exceed that of the lower speed component, and potentially could provide considerable magnetospheric braking.

Another unifying characteristic of the X-ray deficiency syndrome is that it affects progressively cooler stars with increasing luminosity. That would be expected if the relative depth of the convection zone plays an important role. Indeed, the transformation between the coronally deficient and X-ray normal giants appears to occur so abruptly at the G0 break that one suspects a sudden switch in Dynamo modes—or in magnetic loop production mechanisms—which might accompany a critical change in convection zone properties. Giampapa & Rosner (1984) have discussed the latter possibility in some detail for the possibly related case of the early-F dwarfs.

6. SUMMARY AND CONCLUSIONS

Our RIASS Coronathon was designed to survey the coronal, TZ, and chromospheric properties of a large minimally biased sample of F-K stars. We developed specialized processing and measurement schemes to ensure uniform treatment of the observations. Our intent was to explore the behavior of different classes of stars in flux-flux and flux-ratio diagrams. A subsidiary goal was to assess the secular variability of representative stars in the key C IV and Mg II *h* emissions. From our efforts we draw the following conclusions:

1. Coronal activity becomes progressively more sensitive to spectral type as one moves away from the main sequence. On the MS, solar-like coronal activity is ubiquitous for stars later than about mid-F. In the giant branch, solar-like coronae are bounded on the warm side by the X-ray deficiency line near

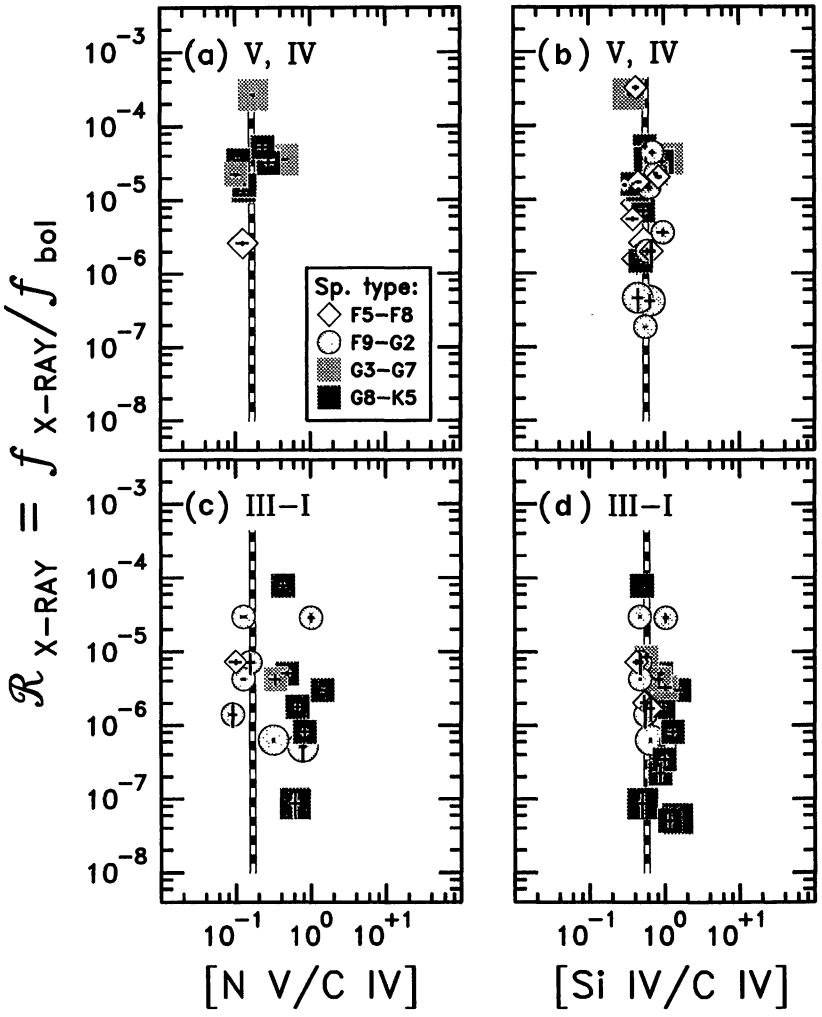

FIG. 17

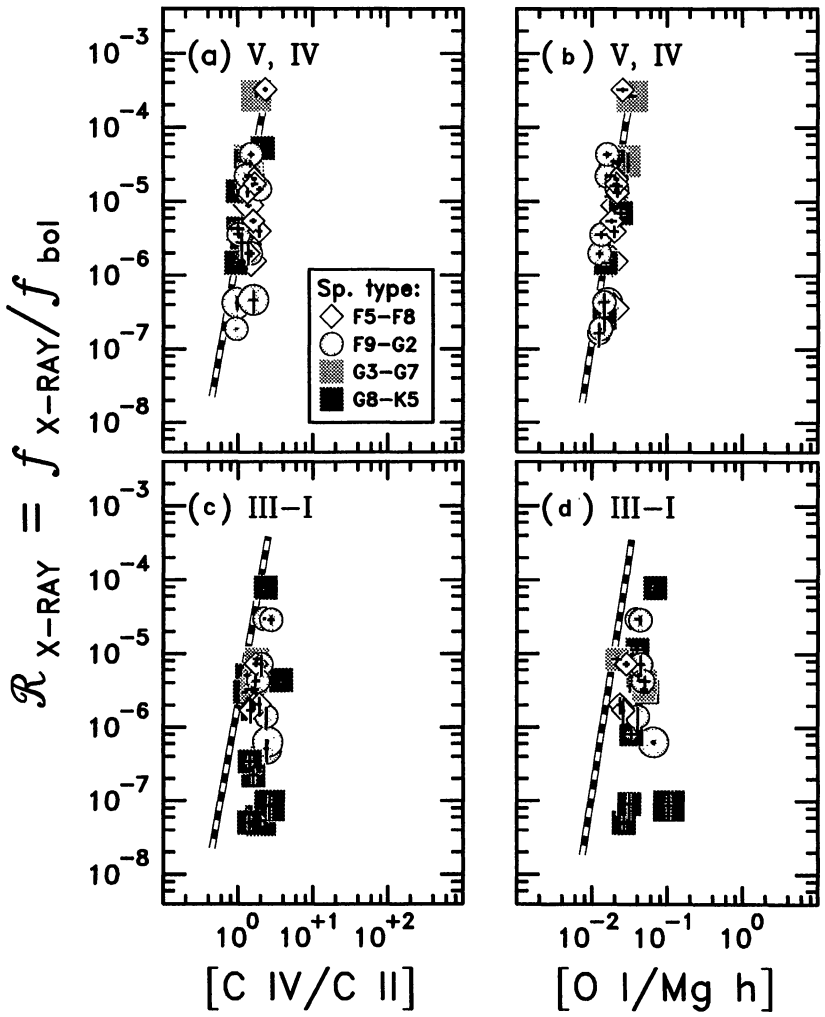

FIG. 18

FIG. 17.—Flux-Ratio diagrams: X-rays vs. (*a,c*) N V/C IV and (*b,d*) Si IV/C IV. We again assign coarser luminosity bins, although here we size code within them [i.e., the smaller symbols in (*c*) are class III giants, and the larger symbols are supergiants (II, I)]. Only ratios significant at the 5 σ level, or better, were used. The (vertical) dashed lines indicate a proposed trend defined by the F9-K5 MS stars.

FIG. 18.—X-rays vs. (*a,c*) C IV/C II and (*b,d*) O I/Mg II *h*. These comparisons involve species of somewhat different excitation as reflected by the tilted MS relations.

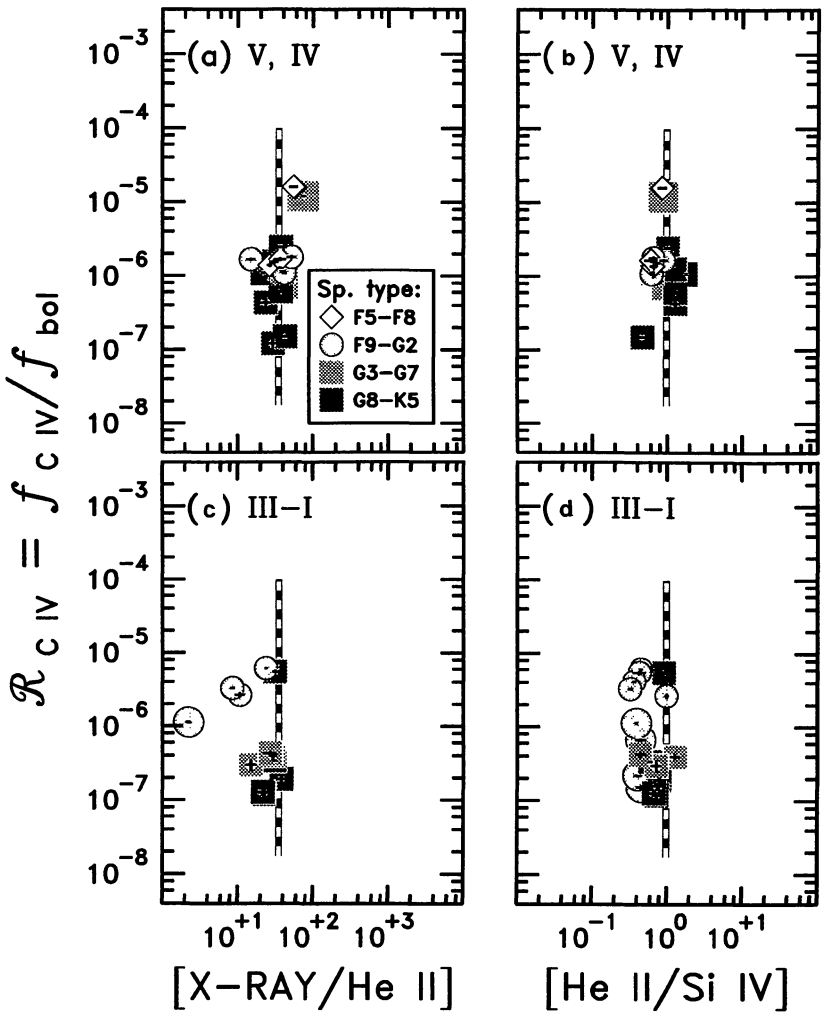

FIG. 19.—C IV vs. (*a,c*) X-rays/He II and (*b,d*) He II/Si IV. He II is a "coronal proxy" whose collisional equilibrium temperature is close to that of Si IV.

G0, and on the cool side by the LH line just beyond K0. In the supergiants, the X-ray deficiency zone has encompassed virtually all of the single stars. The blue side of the zone might be further subdivided by a gross change in the coronal heating mechanism (acoustic to magnetic), a discrete switch in Dynamo modes, or the development of an energy drain such as a fast coronal wind.

2. The moderately active single dwarfs and giants are not more, or less, variable than their quieter counterparts. Indeed, the apparent trend is that cooler stars, whether dwarfs or giants, are more variable than warmer ones (in Mg II, at least). Even for the most variable objects, the secular spread in C IV or Mg II is much smaller than the wide dispersion in activity at that temperature and luminosity. In the simplest solar analogy, active stars are more covered with magnetic plage-like regions than quiet stars. Thus one expects relatively weak rotational modulations in very quiet stars. Their surface emission would be dominated by a minimal magnetic *network* (see, e.g., Skumanich et al. 1984). One expects moderate-to-strong modulations in stars of middling activity. For these, partial coverage by active regions could create significant contrast between one hemisphere and the other. By the same token, one expects weak modulations in the most active stars. Their surfaces would be completely covered by plages (i.e., "saturation": see, e.g., Vilhu 1987). The apparent departure of real stars from that variability scenario, and the existence of the nonlinear flux-flux relations, are important cautions against the literal application of the solar analogy (cf., Oranje 1983; Simon 1984).

3. In some moderate-mass giants, coronal activity can be sustained well after the G0 break, close to the LH dividing line. Examples are the active Clump giants θ^1 Tau and β Cet, and the more dramatic case of the fast rotating Li-rich single K giants. At the other extreme lies the K giant Arcturus, falling below extrapolations of even the X-ray deficient track.

4. Most classes of stars, in the X-ray deficient zones or not, show a wide range of coronal activity. Such diversity is the hallmark of magnetic activity. For example, the active G su-

pergiants and their hybrid cousins have dramatically different FUV intensities and Mg II profiles. Yet, all of these stars fall along a coherent C IV/Mg II locus, and probably X-ray/C IV as well. Their activity appears to be as "connected" as that of the MS stars. The same can be said of the Clump giants as a group. Thus, "hybrid" stars should not be viewed a distinct class. They simply are lower in coronal activity in the same way that the Sun or α Cen A are much less active than χ^1 Ori or π^1 UMa.

The coherence of the flux-flux relations strongly implicates the role of *coronal evolution.* The Dynamo thrives on at least one fundamental stellar parameter—i.e., rotation—that either is negatively affected by the activity itself (e.g., magnetospheric spindown), or depends naturally on the evolutionary state (through changes in the moment of inertia and internal redistributions of angular momentum).

The wide dispersion in coronal activity highlights the crucial, albeit indirect, role of the stellar mass. It sharply delimits the evolutionary interval over which magnetospheric drag can act on the stellar spin. The more massive stars have short lives, and only brief incursions into the magnetoconvective zone of the H-R diagram. Conversely, low-mass stars shed angular momentum throughout their long MS lifetimes. Furthermore, the inflationary first ascent of the giant branch occupies a significant span for $M \lesssim 1.5\ M_\odot$ stars like Arcturus, whereas most of the more massive giants will be found in the postdeflation Clump phase (e.g., Lattanzio 1986; Renzini et al. 1992). Nevertheless, the protracted residence in the CHeB Clump for moderate-mass stars is completely analogous to the long hydrogen burning MS phase for lower mass stars. The shorter chronological interval in the Clump is compensated by the fast magnetospheric spindown times for giants (e.g., Schrijver & Pols 1993).

Above all, the existence of distinct activity loci in the flux-flux diagrams is provocative. The organized structure undoubtedly reflects a common link among the diverse inhabitants of the coronal zoo. We have powerful observational tools like *HST, EUVE, ROSAT, ASCA,* and the venerable *IUE* to explore the associated elusive puzzles of mass loss, spin-down, and coronal heating. Nevertheless, much hard work lies ahead to solidify the present unsteady foundation of speculation.

This work was supported by the National Aeronautics and Space Administration through grants NAG5-199, NAG5-1215 and NAG5-1791 to the University of Colorado. The ROSAT project is supported by the German Bundesministerium für Forschung und Technologie (BMFT/DARA) and the Max Planck Society. We particularly thank C. Imhoff and L. Rossi for their help with the project. We also thank F. Fekel, D. Gray, and K. Schrijver for illuminating discussions concerning spindown in the Hertzsprung gap and beyond. We extensively utilized the SIMBAD database, operated by the Centre de Donnees Astronomiques de Strasbourg.

REFERENCES

Athay, R. G. 1988, ApJ, 329, 482
———. 1988, ApJ, 331, 467
———. 1993, PASP, 105, 538
Ayres, T. R., Brown, A., Gayley, K. G., & Linsky, J. L. 1993, ApJ, 402, 710
Ayres, T. R., Fleming, T. A., & Schmitt, J. H. M. M. 1991, ApJ, 376, L45
Ayres, T. R., & Kashyap, V. 1994, in ASP Conf. Ser., Vol. 64, Cool Stars, Stellar Systems, and the Sun: 8th Cambridge Workshop, ed. J.-P. Caillault (San Francisco: ASP), 681
Ayres, T. R., & Linsky, J. L. 1980, ApJ, 241, 279
Ayres, T. R., Linsky, J. L., Garmire, G., & Cordova, F. 1979, ApJ, 232, L117
Ayres, T. R., Linsky, J. L., Vaiana, G. S., Golub, L., & Rosner, R. 1981, ApJ, 250, 293
Ayres, T. R., Marstad, N. C., & Linsky, J. L. 1981, ApJ, 247, 545 (AML)
Ayres, T. R., Schiffer, F. H., III., & Linsky, J. L. 1983, ApJ, 272, 223
Baliunas, S. L., & Vaughan, A. H. 1985, ARA&A, 23, 379
Basri, G., Clarke, J. T., & Haisch, B. M. 1985, A&A, 144, 161
Bennett, J. O. 1987, Ph.D. thesis, University of Colorado
Bennett, J. O., & Ayres, T. R. 1988, PASP, 100, 1129
Boesgaard, A. M., & Simon, T. 1984, ApJ, 277, 241
Boggess, A., et al. 1978, Nature, 275, 372
Bohlin, R. C., & Grillmair, C. J. 1988, ApJS, 66, 209
Böhm-Vitense, E., & Mena-Werth, J. 1991, ApJ, 378, 718
———. 1992, ApJ, 390, 253
Bopp, B. W., & Fekel, F. 1977, AJ, 82, 490
Brown, A., Drake, S. A., Van Steenberg, M. E., & Linsky, J. L. 1991, ApJ, 373, 614
Carlsson, M., & Judge, P. G. 1993, ApJ, 402, 344
Catura, R. C., Acton, L. W., & Johnson, H. M. 1975, ApJ, 196, L47
Cruddace, R. G., Hasinger, G., Trümper, J., Schmitt, J. H. M. M., Hartner, G. D., Rosso, C., & Snowden, S. L. 1991, Experimental Astron., 1, 365
de Martino, D., Wamsteker, W., Mas Hesse, J. M., Bonnell, J., & Imhoff, C. 1991, NASA *IUE* Newsletter, 46, 71
Dempsey, R. G., Linsky, J. L., Fleming, T. A., & Schmitt, J. H. M. M. 1993, ApJS, 86, 599
Dravins, D., Linde, P., Fredga, K., & Gahm, G. F. 1993, ApJ, 403, 396
Dupree, A. K. 1975, ApJ, 200, L27
Fekel, F. C., & Balachandran, S. 1993, ApJ, 403, 708
Fekel, F. C., & Marschall, L. A. 1991, AJ, 102, 1439
Fisher, P. C., & Meyerott, A. J. 1964, ApJ, 139, 123
Garhart, M. P. 1992, NASA *IUE* Newsletter, 48, 80
Giampapa, M. S., & Rosner, R. 1984, ApJ, 286, L19
Gray, D. F. 1991, in Angular Momentum Evolution of Young Stars, ed. S. Catalano & J. R. Stauffer (Dordrecht: Kluwer), 183
Haisch, B. M., Linsky, J. L., Weinstein, A., & Shine, R. A. 1977, ApJ, 214, 785
Haisch, B. M., Schmitt, J. H. M. M., & Fabian, A. C. 1992, Nature, 360, 239
Haisch, B. M., Schmitt, J. H. M. M., & Rosso, C. 1991, ApJ, 383, L15
Haisch, B. M., & Simon, T. 1982, ApJ, 263, 252
Hallam, K. L., Altner, B., & Endal, A. S. 1991, ApJ, 372, 610
Hallam, K. L., & Wolff, C. L. 1981, ApJ, 248, L73
Hartmann, L., Davis, R., Dupree, A. K., Raymond, J., Schmidtke, P. C., & Wing, R. F., 1979, ApJ, 233, L69
Hartmann, L., Dupree, A. K., & Raymond, J. C. 1980, ApJ, 236, L143
———. 1981, ApJ, 246, 193
Hartmann, L., Jordan, C., Brown, A., & Dupree, A. K. 1985, ApJ, 296, 576
Hasinger, G. 1985, Inf. Bull. Centre de Données Stellaires, 28, 87
Hoffleit, D., & Jaschek, C. 1982, The Bright Star Catalogue (4th ed.; New Haven: Yale Univ. Obs.)
Johnson, H. L. 1966, ARA&A, 4, 193
Judge, P. G. 1986, MNRAS, 221, 119
Kashyap, V., Rosner, R., Harnden, F. R., Jr., Maggio, A., Micela, G., & Sciortino, S. 1994, ApJ, 431, 402
Kinney, A. L., Bohlin, R. C., & Neill, J. D. 1991, PASP, 103, 694
Kurucz, R. L. 1991, in Solar Interior and Atmosphere, eds. A. N. Cox, W. C. Livingston, & M. S. Matthews (Tucson: Univ. of Arizona Press), 663
Lambert, D. L., & Ries, L. M. 1981, ApJ, 248, 228
Lattanzio, J. C. 1986, ApJ, 311, 708
Lenz, D. D., & Ayres, T. R. 1992, PASP, 104, 1104

Linsky, J. L., & Ayres, T. R. 1978, ApJ, 220, 619
Linsky, J. L., Brown, A., & Carpenter, K. G. 1991, in The First Year of *HST* Observations, ed. A. L. Kinney & J. C. Blades (Baltimore: STScI), 70
Linsky, J. L., & Haisch, B. M. 1979, ApJ, 229, L27 (LH)
Luck, R. E. 1978, ApJ, 219, 148
Luck, R. E., & Lambert, D. L. 1981, ApJ, 245, 1018
Mewe, R., Heise, J., Gronenschild, E. H. B. M., Brinkman, A. C., Schrijver, J., & den Boggende, A. J. F. 1975, ApJ, 202, L67
Middlekoop, F., & Zwaan, C. 1981, A&A, 101, 26
Napiwotzki, R., Barstow, M. A., Fleming, T., Holweger, H., Jordan, S., & Werner, K. 1993, A&A, 278, 478
Noyes, R. W., Hartmann, L. W., Baliunas, S. L., Duncan, D. K., & Vaughan, A. H. 1984, ApJ, 279, 763
Oliversen, N., Perez, M. R., & Garhart, M. 1991, NASA *IUE* Newsletter, 46, 19
Oranje, B. J. 1983, A&A, 124, 43
Parker, E. N. 1970, ARA&A, 8, 1
Pounds, K. A. 1993, MNRAS, 260, 77
Reimers, D. 1984, A&A, 136, L5
Reimers, D., & Schmitt, J. H. M. M. 1992, ApJ, 392, L55
Renzini, A., Greggio, L., Ritossa, C., & Ferrario, L. 1992, ApJ, 400, 280
ROSAT MISSION DESCRIPTION 1991, NASA NRA 91-OSSA-25, Append. F.
Savage, B. D., & Mathis, J. S. 1979, ARA&A, 17, 73
Schaller, G., Schaerer, D., Meynet, G., & Maeder, A. 1992, A&AS, 96, 269
Schmidt, E. G., Rosendhal, J. D., & Jewsbury, C. P. 1974, ApJ, 189, 293
Schmitt, J. H. M. M., Collura, A., Sciortino, S., Vaiana, G. S., Harnden, F. R., & Rosner, R. 1990, ApJ, 365, 704
Schrijver, C. J. 1987, A&A, 172, 111
Schrijver, C. J., & Pols, O. R. 1993, A&A, 278, 51
Simon, T. 1984, Ap&SS, 118, 209
Simon, T., & Drake, S. A. 1989, ApJ, 346, 303 (SD)
Simon, T., Herbig, G., & Boesgaard, A. M. 1985, ApJ, 293, 551
Skumanich, A., Lean, J. L., White, O. R., & Livingston, W. C. 1984, ApJ, 282, 776
Stocke, J. T., Morris, S. L., Gioia, I. M., Maccacaro, T., Schild, R., Wolter, A., Fleming, T. A., & Henry, J. P. 1991, ApJS, 76, 813
Trümper, J. 1983, Adv. Space Res., 2, 241
———. 1992, QJRAS, 33, 165
Turnrose, B. E., & Thompson, R. W. 1984, *International Ultraviolet Explorer* Image Processing Information Manual Version 2.0 (New Software), Computer Sciences Corp. TM-84/6058
Vaiana, G. S., et al. 1981, ApJ, 245, 163
Vaiana, G. S., & Rosner, R. 1978, ARA&A, 16, 393
Vilhu, O. 1987, in Lecture Notes in Physics, Vol. 291, Cool Stars, Stellar Systems, and the Sun, ed. J. L. Linsky, & R. E. Stencel (New York: Springer), 110
Voges, W. 1992, in Space Science with Particular Emphasis on High Energy Astrophysics, ed. T. D. Guyene & J. J. Hunt (Noordwijk: ESA), ISY-3, 9
Wahlstrøm, C. & Carlsson, M. 1994, ApJ, (in press, 20 September)
Walter, F. M., Charles, P. A., & Bowyer, C. S. 1978, AJ, 83, 1539
Wilson, O. C. 1978, ApJ, 226, 379
Wilson, O. C., & Bappu, M. K. V. 1957, ApJ, 125, 661
Wood, B. E., Brown, A., & Linsky, J. L. 1995, ApJ, in press
Wood, B. E., Brown, A., Linsky, J. L., Kellett, B. J., Bromage, G. E., Hodgkin, S. T., & Pye, J. P. 1994, ApJS, 93, 287